

ABSTRACT

JANGALE, VILAS VYANKATRAO. Optical Gas Quality Sensor for Natural Gas and Opportunity Fuels. (Under the direction of Dr. Alexei V. Saveliev).

Today, a variety of fuel mixtures – Natural Gas in various forms (LNG, NGL, CNG, LPG, GTL), Syngas, Biogas – are being used to operate internal combustion engines, turbines and other combustion systems. The composition, and hence energy content of these fuels, changes with geographic location. For process control and optimization, it is necessary to know the properties of the fuel being supplied to a combustion system. Conventional methods used for this purpose are gas chromatography or calorimetry, gas chromatography being almost universally used. These methods require by-pass flow lines and fluid extraction to take sample gas which is then taken to a laboratory at a central location to analyze its properties. This is a time-consuming process and it is not possible to monitor the energy content of the fluid continuously and accurately. Also, gas chromatographs are expensive, need frequent maintenance and skilled operators are needed to operate them. This gives rise to the necessity of a low-cost, faster and user-friendly sensor. A real-time optical gas quality sensor, which utilizes the amount of light absorbed by a multi-compound fuel mixture to predict the composition and heating value, has been developed. An NIR optic system is used to measure the absorption under continuous, flow-through pipeline conditions. The measurements are virtually instantaneous. A commercialized version of this sensor is estimated to cost less than half the price of GCs.

© Copyright 2010 by Vilas Vyankatrao Jangale

All Rights Reserved

Optical Gas Quality Sensor for Natural Gas and Opportunity Fuels

by
Vilas Vyankatrao Jangale

A thesis submitted to the Graduate Faculty of
North Carolina State University
in partial fulfillment of the
requirements for the Degree of
Master of Science

Mechanical Engineering

Raleigh, North Carolina

2010

APPROVED BY:

Dr. William Roberts
Co-Chair of Advisory Committee

Dr. Tiegang Fang

Dr. Russell Philbrick

Dr. Alexei V. Saveliev
Chair of Advisory Committee

DEDICATION

This work is dedicated to my parents, elder brother and sister-in-law. Without their love and support, I wouldn't have been able to achieve my dreams.

BIOGRAPHY

The author was born and brought up in Latur, India. After completing the schooling, he got his bachelor's degree in Mechanical Engineering from SV National Institute of Technology, India and developed an interest in combustion and thermodynamics. Later, he joined the Department of Mechanical and Aerospace Engineering at North Carolina State University, Raleigh to pursue his graduate studies.

ACKNOWLEDGEMENTS

I would like to sincerely thank my advisor, Dr. Alexei Saveliev for his guidance, motivation and support throughout these two years. It was really a nice learning experience working with Dr. Saveliev. I am thankful to Dr. Richard Gould for directing me towards Dr. Saveliev. I would also like to thank Dr. Serguei Zelepouga for his support and motivation during my work at GTI, Des Plaines. Special thanks to Vitaly Gnatenko for performing the tests on landfill gas mixtures and providing the test results. I would also like to thank Dr. Russell Philbrick for giving me access to his Flex lab and MODTRAN software.

I am also thankful to all my friends, who made my stay at NC State enjoyable. I would also like to thank my friends back in India.

Finally, my gratitude goes to my parents, my elder brother and sister-in-law for their unending love and support.

TABLE OF CONTENTS

LIST OF TABLES	viii
LIST OF FIGURES	ix
1. INTRODUCTION AND BACKGROUND	1
1.1 Natural Gas and Opportunity Fuels.....	1
1.2 Conventional Methods for Hydrocarbon Fuel Mixture Analysis.....	1
1.2.1 Calorimetry	1
1.2.2 Gas chromatography	3
1.3 Necessity of a Low Cost, Real-Time Natural Gas and Opportunity Fuel Analyzer ..	6
1.4 Spectroscopy basics.....	8
1.5 Composition of Natural Gas and Landfill Gas.....	18
1.6 Thesis Objectives and Outline.....	19
2. CHARACTERIZATION OF HYDROCARBON FUEL MIXTURES USING NIR SPECTROSCOPY	21
2.1 Beer’s Law	21
2.2 Selection of Spectral Range	24
2.3 Justification of NIR Method.....	26
2.4 Multivariate Analysis of Spectra.....	32
3. EXPERIMENTAL APPROACH	35
3.1 Optical Setup	35
3.2 Data Acquisition System.....	38
3.3 Flow Control System.....	39

3.4	Experimental Procedures.....	41
3.4.1	Spectral Calibration	41
3.4.2	Validation.....	43
3.5	Analysis of the Experimental Error.....	44
4.	LINEARITY OF NIR SPECTRA OF HYDROCARBONS	47
4.1	Spectral Line Broadening and Shift	47
4.2	NIR Spectra of Hydrocarbons and Carbon Dioxide at Elevated Pressures.....	51
4.3	Results and Discussion.....	57
4.4	Correcting the NIR Spectra for STP Conditions	64
4.5	Characterization of Landfill Gas Flowing at Elevated Pressures.....	66
5.	ACCOUNTING FOR COMPRESSIBILITY OF HYDROCARBON FUELS.....	68
5.1	Compressibility of Hydrocarbons Mixtures.....	68
5.2	Compressibility of Hydrocarbons–Carbon Dioxide Mixtures	70
5.3	Predicting the Concentrations of NIR Inactive Components in a Fuel Mixture	76
5.4	Experimental Determination of the Compressibility Factor of Hydrocarbon Mixture	
	78	
6.	MINIMIZING TEMPORAL DRIFT OF SPECTRAL DETECTOR	81
6.1	Determining the Repeatability of Spectral Measurements.....	81
6.1.1	Experimental Approach	81
6.1.2	Experimental Procedure.....	82
6.1.3	Results and Conclusion.....	83
6.2	Effect of Optical Instabilities on Prediction Error	84
6.3	Temporal Drift in Spectra due to Optical and Electronic Instabilities.....	85

6.4	Drift Correction	89
CONCLUSIONS	96
FUTURE WORK	98
REFERENCES	99
APPENDICES	106
APPENDIX A1	107

LIST OF TABLES

Table 1. Natural gas analyzers [1 – 13].	4
Table 2. Typical composition of natural gas [21].	18
Table 3. Typical composition of landfill gas [22].	19
Table 4. Natural gas pipeline diameters [31].	51
Table 5. Laboratory measurement conditions.	54
Table 6. Calibration matrix used for validation of density correction algorithm.	66
Table 7. Multipole factor as a function of acentric factor and carbon dioxide concentration.	74
Table 8. Average absolute percent prediction error.	85

LIST OF FIGURES

Fig. 1.1 The electromagnetic spectrum.....	10
Fig. 1.2 Transitional diagram of a rotation-vibration spectrum [18]	15
Fig. 1.3 IR regions for fundamental vibrational modes of different types of bonds [19].....	16
Fig. 1.4 Absorption and emission of a photon	17
Fig. 2.1 IR absorption spectra of natural gas components (a) linear and (b) logarithmic absorbance scale [28]	27
Fig. 2.2 Synthetic NIR absorption spectra of methane and carbon dioxide (a) linear (b) logarithmic absorbance scale	29
Fig. 2.3 Individual low resolution NIR spectra of C1 to C4 hydrocarbons and carbon dioxide measured in 50 cm path length at atmospheric pressure and temperature are shown with linear (above) and log (below) scales	31
Fig. 2.4 Model structure of PCR and PLS [30].....	34
Fig. 3.1 Overall layout of experimental setup.....	36
Fig. 3.2 Optical setup of gas quality sensor	38
Fig. 3.3 Schematic of data acquisition system.....	39
Fig. 3.4 Pin diagram for connecting flow control system to data acquisition system	41
Fig. 3.5 Example of a typical prediction testing result	46
Fig. 4.1 Linearity in the density with pressure ($Z \sim 1$)	55
Fig. 4.2 NIR absorption spectra at elevated pressures for (a) methane (b) propane (c) carbon dioxide.....	56

Fig. 4.3 Linearity of NIR absorption with density for (a) methane (b) propane and (c) carbon dioxide.....	59
Fig. 4.4 Linearity in absorbance with density at selected wavelengths for (a) methane (b) propane and (c) carbon dioxide.....	61
Fig. 4.5 NIR spectra scaled down to ambient pressure for (a) methane (b) propane and (c) carbon dioxide.....	63
Fig. 4.6 Schematic flow diagram of fuel properties calculation procedure	65
Fig. 4.7 Prediction accuracy of density correction algorithm (a) methane (b) carbon dioxide (c) heating value.....	67
Fig. 5.1 SBV T_{pc} minus graphically determined T_{pc} as a function of concentration of carbon dioxide [23].....	72
Fig. 5.2 Multipole factor versus hydrocarbon acentric factor for 5 to 50% CO ₂ [23].....	72
Fig. 5.3 Multipole factor versus hydrocarbon acentric factor for 60 to 90 % CO ₂ [23].....	73
Fig. 5.4 Polynomial curves fitting for numerical determination of multipole factor.....	75
Fig. 5.5 Schematic flow diagram of procedure for correcting the compressibility factor programmatically	78
Fig. 5.6 NIR absorption spectrum of a mixture of 33.96% methane, 42.45% propane and 23.58% nitrogen at 8.78 bar and 300 K	79
Fig. 6.1 Optical setup to determine repeatability of spectral measurements	82
Fig. 6.2 Example of a typical temporal drift distribution of a sensor during 11 days of measurement	83
Fig. 6.3 Percentage error in measured absorbance	84

Fig. 6.4 Prediction error	85
Fig. 6.5 Example of a typical temporal drift of a NIR detector based on repeated measurements.....	87
Fig. 6.6 Lineplot with drifting response signals during four days of measurement (Sequence 1 – 4)	88
Fig. 6.7 Temporal drift in the reference intensity	89
Fig. 6.8 Drift correction of measured spectra	92
Fig. 6.9 Drift correction in multisequence measurements	93
Fig. 6.10 Reference intensity I_0	94
Fig. 6.11 Reference intensity reconstruction	95
Fig. A1. 1 Absorbance correction VI - connector pane	108
Fig. A1. 2 Main UI - front panel.....	109
Fig. A1. 3 Absorbance correction VI - front panel	110

1. INTRODUCTION AND BACKGROUND

1.1 Natural Gas and Opportunity Fuels

Today in the US and other countries, commercial and industrial combustion systems, such as, combined heat and power (CHP) and distributed generation (DG) systems, combined cycle plants, microturbines, fuel cells and advanced internal combustion engines, are utilized for energy production and distribution. Natural gas is the fuel of choice for most CHP and emerging DG technologies. Other typical DG/CHP fuels include diesel, propane, and increasingly, ‘opportunity fuels’ such as biogas from landfill operations. For improved process control and optimum utilization of these combustion systems, it is necessary to monitor the composition and energy content of the fuel. There exist a number of energy content measurement devices in the industry. A few of them and their principles of operation are described below.

1.2 Conventional Methods for Hydrocarbon Fuel Mixture Analysis

The science of heating value measurement has seen revolutionary changes starting from gas calorimeters to sophisticated gas chromatographs, which directly measure the composition. Gas chromatography is almost a universally preferred method nowadays. These methods are discussed below.

1.2.1 Calorimetry

Calorimetry is the process of measuring the heat of chemical reactions. The word calorimetry is derived from the Latin word *calor*, meaning heat. Constant volume calorimetry measures the internal energy change between reactants and products, but constant pressure calorimetry

measures directly the enthalpy change during the reaction. These two heats are slightly different when gases are evolved or consumed during the transformation. Heat evolved during a reaction changes the temperature of a working substance (e.g. water bath) with a known heat capacity. Thus a measurement of temperature rise in the surroundings allows determination of the heat crossing the system boundary. The heat evolved is given by Eq. (1.1).

$$q = m c \Delta T \quad (1.1)$$

Where q is the heat, m is the mass, c is the specific heat capacity and ΔT is the change in temperature. In constant volume calorimetry (bomb calorimetry), no work is performed and hence the heat measured equals the change in internal energy of the system.

$$q = m C_v \Delta T = m \Delta U \quad (1.2)$$

Where C_v is the specific heat capacity at constant volume and ΔU is the change in internal energy. Indirect calorimetry estimates energy expenditure by measuring the amount of oxygen consumed or carbon dioxide released. Calorimeters, used for measurement of natural gas energy content, generally use indirect calorimetry. In this method, the oxygen content in the flue gas after combustion of the sample is measured. A gas sample is continuously mixed with dry air. The fuel-air mixture is oxidized in a combustion furnace, sometimes in the presence of a catalyst and the concentration of oxygen in the combusted sample is measured [1]. Sometimes, a constant exhaust temperature is maintained by precisely regulating the combustion air supplied (i.e. lower air flow when heating value is higher and higher air flow

when heating value is lower). The air flow is monitored and heating value of the gas sample is estimated [2].

1.2.2 Gas chromatography

In gas chromatography (GC), the mobile phase is a gas; usually an inert gas such as helium or an unreactive gas such as hydrogen, nitrogen and the stationary column has a microscopic layer of liquid or polymer on an inert solid support, inside glass or metal tubing. The instrument used to perform gas chromatographic separations is called a *gas chromatograph* (also *aerograph*, *gas separator*). The mixture to be analyzed is dissolved in the mobile phase and is passed through the stationary phase, in which different compounds elute at different times called retention time. The retention time allows in identification of a component and peak area in the chromatogram indicates its amount. There are a significant number of GC products available in the market including the GCs specifically designed for measuring the energy content of natural gas.

Apart from calorimetry and gas chromatography, other techniques used for analyzing the energy content of natural gas mixtures are photometry, speed of sound correlation and microelectromechanical systems. Table 1 gives an overview of the devices based on these techniques.

Table 1. Natural gas analyzers [1 – 13].

		Span	Repeatability	Accuracy	Response time	Disadvantages
Calorimetry	BTU Analyzer COSA 9600™	Wobbe index 0-2730 BTU/SCF	±0.7 BTU/SCF	±0.4% for natural gas, ±2.0% for refinery gases		Short temperature range 10 to 40 degree C (50 to 104 F); Drift: 0.4 BTU/SCF/24 hours
	Tru-Therm H Gas Penetrator Calorimeter by Precision Gas Instruments Inc.	700 - 1750 BTU	1/10 percent of Measured Value (1 BTU)			Limited BTU range
	Flo-Cal High-Speed Calorimeter by Thermo Electron Corporation	Low range: <1500 BTU/scf and High range: >1500 BTU/scf	Low Range=±1.0% of full scale value; high Range=±1.2% of full scale value	± 1.0% of full scale value High range = ± 1.5% of full scale value	Low range = 1.5 minutes plus sample transport time; High range = 3.5 minutes plus sample transport time	costly, 10K +, not real time - tens of seconds – 3 min, cannot be used to measure mixture components
Gas chromatography	ABB Totalflow NGC 8200	N/A	±0.25 Btu @ 1,000 Btu (±0.025%) over temperature range of 0 to 131°F (-18 to 55°C)	0 to 131°F (-18 to 55°C)	5 min	Long cycle time (5 min)
	FXi Series5™ by Applied Instrument Technologies	N/A		-15 to 50 C (5 to 122 F)		Max. supply pressure is 414 kPa (60psi), Chromatographic grade (CG) required
	Agilent 7890A	N/A	< 0.008%	4 °C to 450 °C.		999.99 min (16.7 h)
	HGC303 by COSA Inc	N/A	0.05%	14°F to 122°F (-10°C to 50°C)	5 min	Long cycle time (5 min); 7 to 70 psig measured at flow meter inlet, co-existing component limits: H2, He, O2, H2S (dry) < 0.1 mol% each, ~ \$20K, moisture 2000 ppm or less

Table 1 Continued

Gas chromatography	Daniel® Danalyzer™ Models 570/571	N/A	+/- 0.05% CV		4 min	20K+, analysis cycle time 2 to 12 minutes, require well trained personal for maintenance and operation
Speed of sound correlation	GasPT by Advantica	942 to 1143 BTU/SCF	±0.04 MJ/m³, ±1.1 BTU/SCF	±0.20 MJ/m³, ±5.4 BTU/SCF	50 seconds at 1 litre/min purge rate	price ~ \$18,000
MEMS	Siemens Natural Gas Analyzer SITRANS CV		< 0.01%	< 0.1%	Response time < 180 seconds Temperature range -20 to 55 C	
	Spectra Sensors SS3000 Dual Channel CO2 Analyzer	0-10% CO2	±1% of reading, or ±0.04% (400 ppmv), whichever is greater		0.25-2 seconds	Costly ~ USD 34292.00
Photometry	X-Stream General Purpose Compact Gas Analyzer		< 1%		Response time 4 s to 7 s Temperature range 0 to +50°C (32 to 122°F)	Limited flow range: 0.2 - 1.5 l/min, maximum gas pressure < 1,500 hPa abs. (< 7 psig)
Infrared absorption	GEM™2000 by LANDTECH	Methane 0-100%; Carbon Dioxide 0-60% Oxygen 0-25%		Full Scale methane ±3.0% (100%), ±3.0% (60%), ±1.0% (21%)	Response time ≤ 20 seconds	Low accuracy

1.3 Necessity of a Low Cost, Real-Time Natural Gas and Opportunity Fuel Analyzer

It is clear from Table 1 that the devices/methods presently used in the industry are very expensive and have significant disadvantages. Though the most widely used gas chromatographs are very accurate in predicting the gas composition and heating value, they have some drawbacks:

- They are very expensive (usually more than USD 20,000).
- Need frequent maintenance
- Skilled operators are needed to operate them.
- Long response times, often more than 5 minutes. Hence they do not give essentially real-time information.
- Require fluid extraction for sample from the high pressure pipeline.

Due to the high cost, it is not feasible to install GCs at all the end-user locations. However, they are often installed at a central measurement location, where there is a sufficient operating volume of natural gas to justify the cost. In most cases, this minimum volume translates to about 25 to 30 MMSCFD (Million Standard Cubic Feet per Day) [14]. The average heating value for the gas composition determined at this location is multiplied by the flow rate to calculate the energy delivered at the end-user location. For improved process control and optimum utilization of combustion systems, it is necessary to know the properties of the fuel at the end-user location. Research efforts are being made to shrink the GC technology, however, no significant reduction in price or analysis time is anticipated at this time. Thus, there is the need for an alternative low-cost, real-time fuel analyzer.

In the past few decades, NIR spectroscopy has emerged as a promising technique for hydrocarbon fuel characterization. It has been shown that NIR spectra of hydrocarbon fuels can be correlated to the fuel properties [15]. The proposed method works on the principle of NIR absorption spectroscopy, which is a cost-effective and easy-to-operate alternative method to gas chromatography. The properties of hydrocarbons can be predicted in real-time and *on line*. Beer's law and multivariate calibration techniques are utilized to compare the NIR data of known and unknown gas mixtures and the properties of unknown mixtures are predicted. The sample mixtures for calibration are selected to cover the natural range of variability of mixtures to be tested. The quality of the resulting calibration equation depends upon the number of samples used for calibration and how these samples are selected. The method has the following advantages:

- The method is applicable in a wide range of pressure, temperature and flow rate.
- The results are virtually instantaneous.
- Real-time, continuous prediction of composition and heating value is obtained.
- The spectroscopic setup is very simple to design and operate.
- Rugged construction and no moving parts.
- High accuracy ($\pm 0.5\%$).
- A commercialized version of this sensor is estimated to cost less than half the price of gas chromatographs.

Despite these numerous advantages compared to gas chromatographs or calorimeters, the sensor needed several improvements in regards to the following functions:

- It needs to be calibrated at a constant pressure and temperature.
- The pressure and temperature of the fuel during calibration and testing needs to be the same.
- The sensor cannot predict the concentration of NIR inactive gases present in the mixture, including carbon dioxide.
- The compressibility factor Z of the mixture is not taken into consideration. The compressibility factor becomes significant at elevated pipeline pressures.
- Temporal drift in the absorbance measurements can occur due to variation in the light source temperature and hence reference intensity, background noise level and detector sensitivity drift.

1.4 Spectroscopy basics

Spectroscopy or spectrometry is a technique used in physical or analytical chemistry to determine the concentration of chemical species from their absorption or emission spectra. Each and every species has a unique absorption spectrum depending on their molecular structure and the amount of absorption depends on the concentration of the species. Spectroscopy involves the study of the interaction of electromagnetic radiation (light) with living or non-living matter and how this interaction affects the intensity of light as a function of wavelength (λ) or frequency (ν). The electromagnetic spectrum of a source comprises of the entire range of frequencies that the source emits. This optical portion of the spectrum shown in Fig 1.1 can extend from far infrared to far ultraviolet. A suitable spectral region in

which the substance absorbs light is selected for analysis purpose. Light is allowed to pass through the analyte and the transmitted intensity is measured in the selected spectral region.

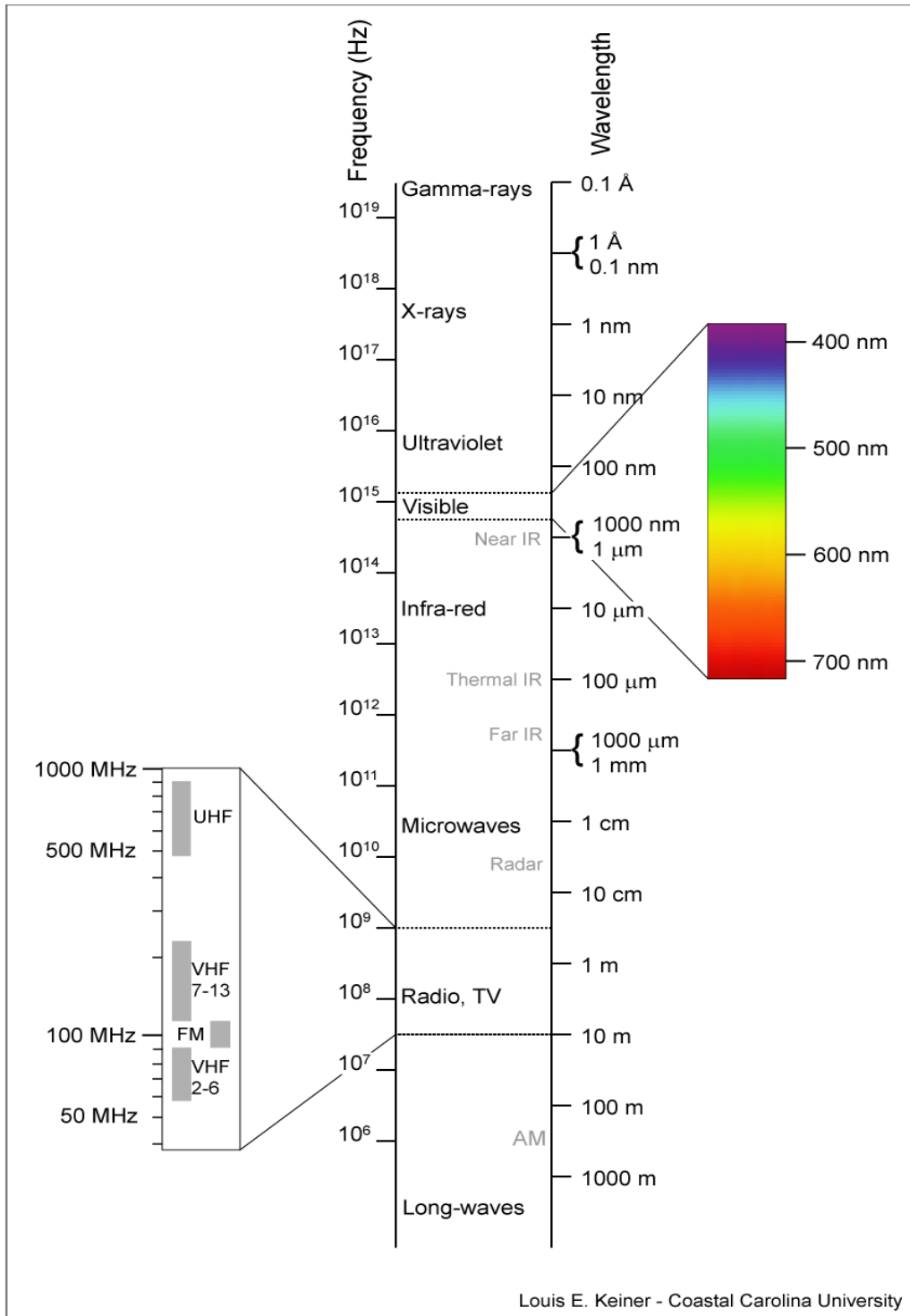


Fig. 1.1 The electromagnetic spectrum

The energy of a molecule can be expressed as the sum of rotational, vibrational and electronic energy.

$$E = E_{rot} + E_{vib} + E_{el} \quad (1.3)$$

Rotational energy is of the order of a few hundredths of an electron volt, vibrational energy is of the order of tenths of an electron volt and electronic energy is of the order of a few electron volts. Molecular spectra can be divided into pure rotation, rotation–vibration or electronic spectrum. Pure rotation spectrum involves transitions between rotational energy levels only; rotation–vibration spectrum involves transitions between the rotational and vibrational energy levels but no electronic energy level transitions; while electronic spectrum is a result of transition between electronic energy levels. Pure rotational spectrum lines lie in the far (or longwave) infrared or microwave region; rotation–vibration spectrum lies in the middle range of the infrared region and electronic spectrum lies in the visible and ultraviolet regions.

Rotational Energy Levels: The rotational kinetic energy of a molecule, E_{rot} , is defined depending upon the geometry of the molecule, which can be linear, spherical-top, symmetrical-top or asymmetrical-top. For linear or spherical-top molecules,

$$E_{rot} = J(J + 1)Bhc \quad (1.4)$$

where,

$$B = \frac{h}{8\pi^2 c I} \quad (1.5)$$

and

$$J = 0, 1, 2, \dots$$

The term, J , is called rotational quantum number, I is the moment of inertia of the molecule about the axis of rotation, h is Planck's constant and c is the speed of light.

For symmetrical-top molecules, an additional quantum number is, K , is required to define the rotational energy levels,

$$E_{rot} = J(J+1)Bhc + K^2(C-B)hc \quad (1.6)$$

where,

$$B = \frac{h}{8\pi^2 c I_b} \quad C = \frac{h}{8\pi^2 c I_c} \quad (1.7)$$

I_b is the moment of inertia about the symmetry axis and I_c is the moment of inertia about the perpendicular axis. In the case of an asymmetrical molecule, three quantum numbers are needed to define the energies of quantized states and it involves complicated theory to define the rotational energy levels. The selection rules for rotational transition are,

$$\begin{aligned} \Delta J &= 0, \pm 1 \\ \Delta K &= \pm 1 \end{aligned} \quad (1.8)$$

Vibrational Energy Levels: Photon energies associated at IR wavelengths are not large enough to excite electrons, but may induce vibrational excitations of covalently bonded atoms and groups. Covalent bonds in molecules are like springs, which can be stretched and

bent. If a molecule contains N atoms, there are $3N$ degrees of freedom (or modes of motion) possible. Of these, three modes correspond to translation; three (or two for a linear molecule) correspond to rotation of the molecule itself. This leaves $3N-6$ (or $3N-5$ for a linear molecule) modes of vibrational motion. Vibrational modes are often given names, such as, stretching, bending, rocking, twisting, scissoring. The exact frequency at which a particular vibration occurs is a function of the bond strength and mass of the component atoms. If $\nu_1, \nu_2, \nu_3, \dots$ are frequencies and v_1, v_2, v_3 are vibrational quantum numbers, vibrational energy is given by

$$E_{vib} = \left(v_1 + \frac{1}{2}\right)h\nu_1 + \left(v_2 + \frac{1}{2}\right)h\nu_2 + \dots \quad (1.9)$$

The vibrational transition rule is

$$\Delta v = \pm 1 \quad (1.10)$$

Transitions in which $\Delta v = \pm 2, \pm 3$ are called overtone transitions and are much weaker than the fundamental transition for which $\Delta v = \pm 1$. A homonuclear diatomic molecule, such as, nitrogen (N_2), oxygen (O_2), does not have a permanent electric dipole moment to directly absorb radiation. Thus neither rotational nor vibrational transitions produce an oscillating dipole moment and associated dipole radiation. Hence, homonuclear diatomic molecules do not exhibit rotation or rotation-vibration spectrum. However, in these cases, an induced electric dipole moment can be active as a transient process caused by the electric field of a scattering photon, and this results in Raman scattering processes. The J -selection rule for a

rotation-vibration transition is $\Delta J = 0, \pm 1$. A vibration-rotation spectrum is divided into three branches – *P*, *Q* and *R* branches [17].

$$\Delta J = -1 \quad P \text{ branch}$$

$$\Delta J = 0 \quad Q \text{ branch}$$

$$\Delta J = +1 \quad R \text{ branch}$$

Fig. 1.2 shows a transitional diagram of a rotation-vibration spectrum.

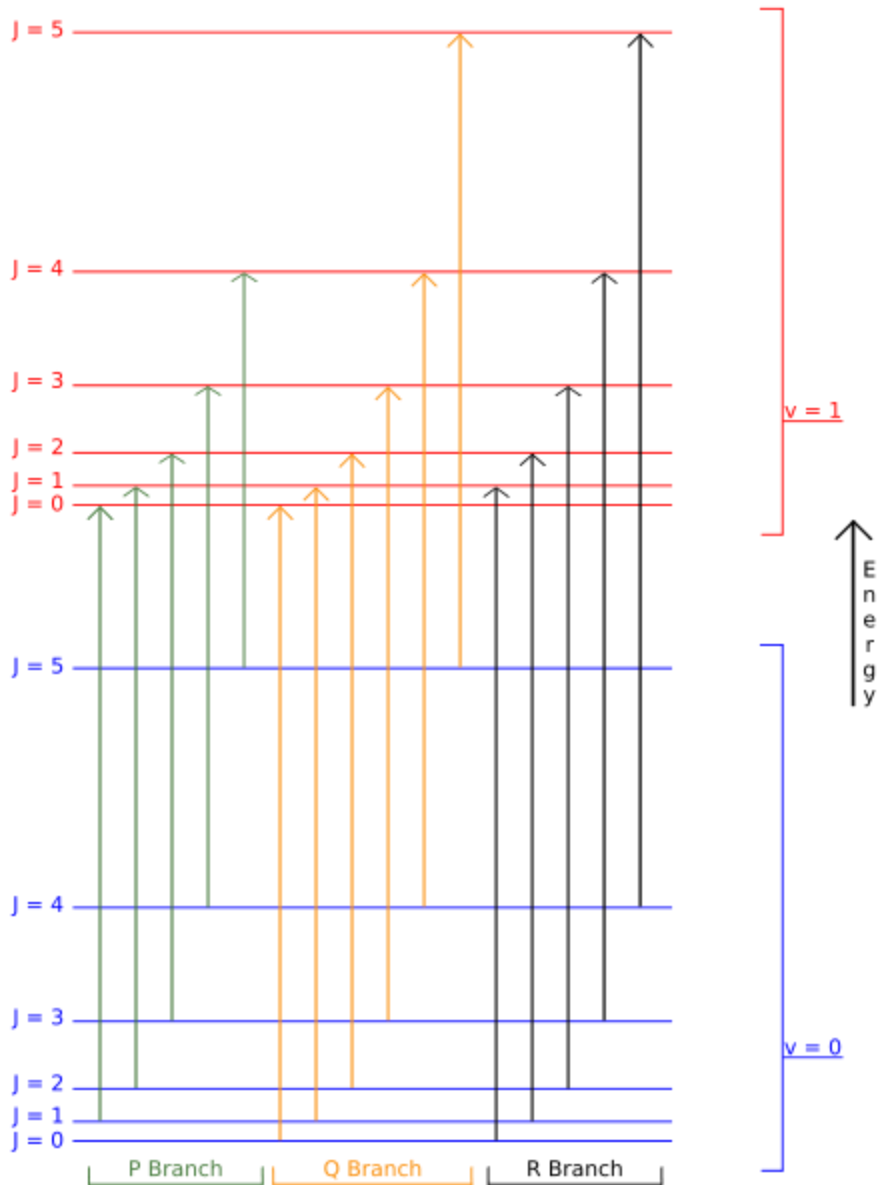


Fig. 1.2 Transitional diagram of a rotation-vibration spectrum [18]

Stretching frequencies are higher than corresponding bending frequencies, i.e., it is easier to bend a molecule than to stretch or compress it. Triple bonds have higher stretching frequencies than corresponding double bonds, which in turn have higher frequencies than

single bonds. Fig. 1.3 shows the infrared regions in which fundamental vibrations of different types of bonds occur.

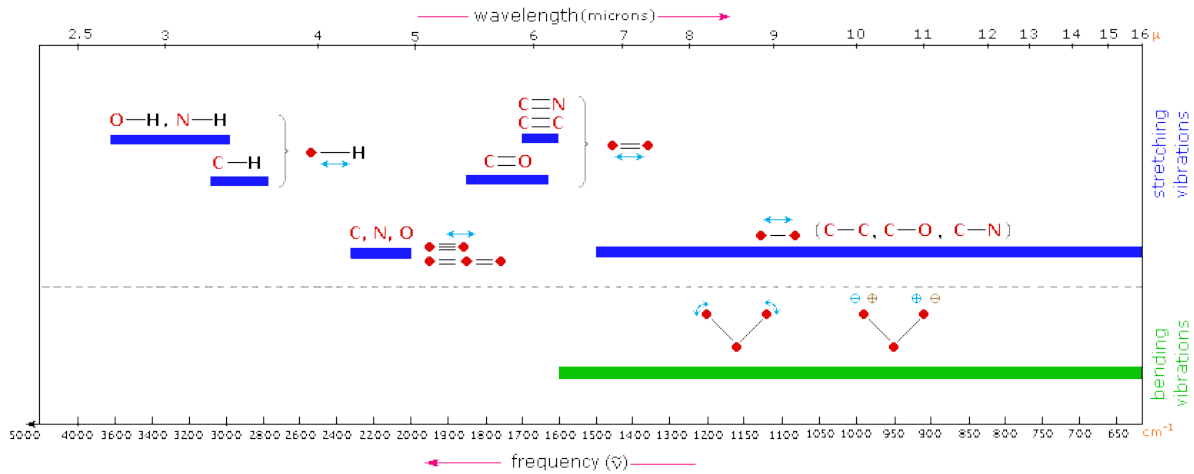


Fig. 1.3 IR regions for fundamental vibrational modes of different types of bonds [19]

Generally prisms or gratings are used to disperse the radiation into a spectrum. The emission spectrum of solid bodies is generally continuous blackbody radiation, however that of atoms or molecules consists of discrete frequencies, usually referred to as the “line” spectrum, and it displays the spectral characteristic of the atoms or molecules involved. The electrons of an atom can occupy only certain discrete quantized states or orbits. When an electron undergoes transition from one energy level to another, it either absorbs or emits energy in the form of electromagnetic radiation whose frequency is given by the Eq. (1.11).

$$\nu = \frac{\Delta E}{h} \quad (1.11)$$

Where ΔE is the energy difference between the two states involved, and h is Planck's constant [20]. Fig. 1.4 shows the processes of photon absorption and emission.

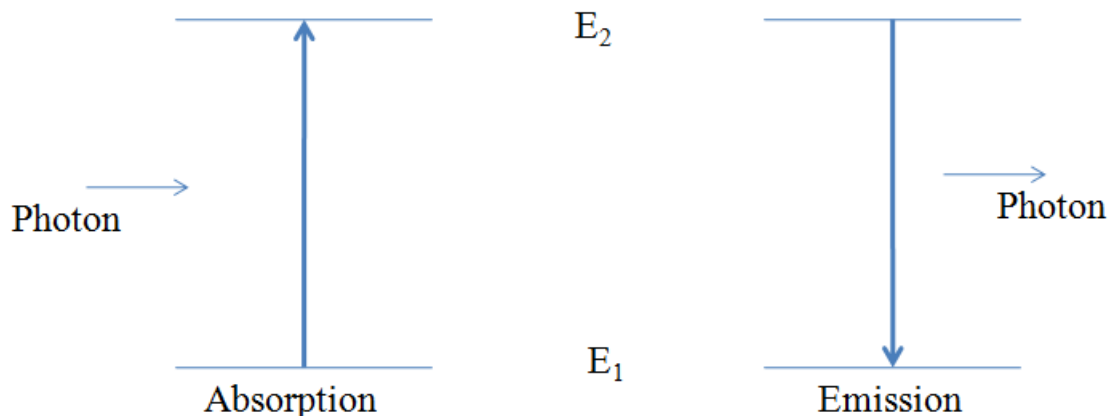


Fig. 1.4 Absorption and emission of a photon

The appearance of spectra (the width and shape of spectral lines) depends upon the resolution of the spectroscopic sensor, concentration of the absorbing species present and the environmental factors (e.g., pressure, temperature and electromagnetic field). With a low resolution spectroscopic instrument, the optical spectra of molecules, particularly diatomic molecules, appear to be formed of more or less regularly spaced bands. On the other hand, with a high resolution instrument, the spectra look like a sequence of closely spaced infinitesimally thin lines. The frequency of an absorption line can be shifted due to interaction of the molecule with neighboring molecules and hence this shift also depends on the pressure and temperature.

1.5 Composition of Natural Gas and Landfill Gas

Most of the hydrocarbon fuels have methane as the primary component. For example, natural gas contains primarily methane and small quantities of higher molecular weight hydrocarbons (C_2 to C_{6+}), carbon dioxide, water vapor and sometimes nitrogen. Biogas, which is practically produced as landfill gas (LFG) consists of primarily methane, carbon dioxide and small quantities of nitrogen, hydrogen, hydrogen sulfide and oxygen. Table 2 and Table 3 give the typical chemical composition of natural gas and biogas respectively. It is clear from Table 2 and Table 3 that the primary component of these fuels is methane. All of these components except nitrogen, oxygen and hydrogen absorb near infrared electromagnetic radiation. The NIR spectra of these components and their suitability for mixture characterization are discussed in *Chapter 2*.

Table 2. Typical composition of natural gas [21].

Component	Range %
Methane	87.0 - 96.0
Ethane	1.5 - 5.1
Propane	0.1 - 1.5
iso - Butane	0.01 - 0.3
normal - Butane	0.01 - 0.3
iso - Pentane	trace - 0.14
normal - Pentane	trace - 0.04
Hexanes plus	trace - 0.06
Nitrogen	0.7 - 5.6
Carbon Dioxide	0.1 - 1.0
Oxygen	0.01 - 0.1
Hydrogen	trace - 0.02

Table 3. Typical composition of landfill gas [22].

Component	Range %
Methane	35–65
Carbon dioxide	35–55
Nitrogen + Oxygen	0–10

1.6 Thesis Objectives and Outline

The current work explores and develops the applications of NIR absorption spectroscopy as an alternative technique to gas chromatography to characterize hydrocarbon fuel mixtures in a wide pressure and temperature range, with a special focus on natural gas and landfill gas (or biogas) mixtures. The thesis outline is organized as follows. *Chapter 2* will provide an insight into the application of NIR spectroscopy (NIRS) to characterize hydrocarbon fuel mixtures. This includes the application of Beer’s law, which is the basis of absorption spectroscopy. The reasons are described for selecting the near-infrared region to determine hydrocarbon mixture analysis. The prerequisites that need to be satisfied in order for Beer’s law to be applicable are examined. Also, the use of multivariate calibration methods – principal components regression and partial least squares – to extract the desired chemical information from the spectra is elaborated. *Chapter 3* discusses the experimental approach for NIR spectroscopy. This includes descriptions of the optical setup, hardware control, high-speed data acquisition system and flow control system. Experimental procedures for spectral calibration and characterization of fuel mixtures are explained. *Chapter 4* includes experimentally measured NIR spectra of methane in the pressure range 1 bar to 13.65 bar (14.69 to 198 psia), propane in the range 1 bar to 8.2 bar (14.69 to 119 psi) and carbon

dioxide in the range 1 to 3.5 bar (~14.69 psi to 50 psi). The pressure range for each gas is chosen considering their maximum mole fractions in natural gas or landfill gas mixtures. The spectral effects of line broadening and associated shift in the line centers due to increase in pressure are discussed. The spectral distribution of NIR spectra of carbon dioxide and hydrocarbons at ambient conditions is studied and the detection of carbon dioxide in a binary methane-carbon dioxide mixture is investigated. Thus the characterization of fuels using NIR spectroscopy is extended to an important fuel class, biogas or landfill gas (LFG), which is nowadays being increasingly used in various combustion systems. It is shown that the NIR spectra recorded at elevated pressures can be correlated to the spectra recorded at ambient conditions. Thus NIR technique is extended to analyze process flow streams for ranges with considerable variations in pressure, temperature and composition. *Chapter 5* discusses the significance of the compressibility factor of natural gas at elevated pressures owing to the presence of highly compressible propane and butane. It is known that the compressibility factor of natural gas-carbon dioxide mixtures or landfill gas have large deviations from the compressibility factors predicted using the most widely used Stewart, Buckhardt and Voo mixing rule. A new technique proposed by Thomas Buxton et al [23] suggesting a correction to the SBV mixing rule and involves graphical determination of pseudocritical properties, which is used to determine the pseudoreduced properties. *Chapter 6* details temporal drift in the NIR spectra due to a combined effect of optical instabilities associated with variation in light source temperature and hence intensity, background noise level and detector sensitivity drift.

2. CHARACTERIZATION OF HYDROCARBON FUEL MIXTURES USING NIR SPECTROSCOPY

2.1 Beer's Law

Beer's law, also known as Beer–Lambert law, states that there is a logarithmic dependence between the incident and transmitted intensity and depends on the concentration of absorbing species and the distance light travels through that species. Mathematically,

$$T(\lambda) = \frac{I(\lambda)}{I_0(\lambda)} = e^{-\varepsilon(\lambda)lc} \quad (2.1)$$

Where $T(\lambda)$ is the transmittance, $I(\lambda)$ is the intensity of light transmitted through the specie and $I_0(\lambda)$ is the intensity before it enters the specie (incident light), $\varepsilon(\lambda)$ is the molar absorptivity at a wavelength λ , expressed in $\text{L mol}^{-1} \text{cm}^{-1}$, l is the distance light travels through the absorbing specie in cm and c is the molar concentration in mol L^{-1} . In quantitative spectroscopy, the absorbance $A(\lambda)$ or optical density (OD) is defined as the ratio of radiant flux absorbed by a specie to that incident upon it. The logarithm base 10 is more commonly used.

$$A(\lambda) = -\log_{10} T(\lambda) = -\log_{10} \left[\frac{I(\lambda)}{I_0(\lambda)} \right] = \varepsilon(\lambda) l c \quad (2.2)$$

Thus, as a consequence, absorbance is directly proportional to the path length and the concentration of absorbing species. Beer's law is the basis for absorption spectroscopy.

$$\begin{aligned} A &= \varepsilon(\lambda) \ell c \\ \text{or } A &= k(\lambda) c \end{aligned} \quad (2.3)$$

The molar absorptivity, also called molar absorption coefficient or molar extinction coefficient, is a measure of how strongly a species absorbs light at a given wavelength. It is an intrinsic property of the specie and is a function of wavelength. If the path length ℓ and molar absorptivity ϵ are known and the absorbance A is measured, the concentration c of the absorbing specie can be determined. The law can be extended to a mixture of several absorbing components, if they act independently. For example, for a mixture of two components, the absorbance measured at a wavelength λ , is given by the Eq. (2.4).

$$A = c_1 k_1(\lambda) + c_2 k_2(\lambda) \quad (2.4)$$

Thus, if the absorbance of the mixture is measured at one more wavelength, we get a system of two equations with two unknowns c_1 and c_2 , which can be solved to compute the unknown concentrations. For more than two components, linear least squares method is used. In general, for a mixture containing n components,

$$A_j = \sum_{i=1}^n c_i k_{ij} \quad (2.5)$$

Where j is the number of wavelengths at which the absorbances of the mixture are measured ($j \geq n$). A_1, A_2, \dots, A_j are the absorbances measured at wavelengths $\lambda_1, \lambda_2, \dots, \lambda_j$; c_1, c_2, \dots, c_n are the molar concentrations of the components and k_{ij} is the molar absorptivity of i^{th} component at j^{th} wavelength. k_{ij} is the molar absorptivity of the i^{th} component at j^{th} wavelength. Equation (2.5) can be written in matrix notation as

$$[A_1 \ A_2 \ \dots \ A_j] = [c_1 \ c_2 \ \dots \ c_n] \begin{bmatrix} k_{11} & k_{12} & \dots & k_{1j} \\ k_{21} & k_{22} & \dots & k_{2j} \\ \vdots & \vdots & & \vdots \\ k_{n1} & k_{n2} & \dots & k_{nj} \end{bmatrix} \quad (2.6)$$

Where matrix A contains spectral absorbance data, matrix c contains the concentrations and matrix k provides the proportionality between the two. It has been found more useful to use the inverse formulation of Beer's law, so the concentrations are expressed as a function of absorbances. For a three component system, the above matrix formulation becomes

$$[c_1 \ c_2 \ \dots \ c_n] = [A_1 \ A_2 \ \dots \ A_j] \begin{bmatrix} p_{11} & p_{12} & \dots & p_{1n} \\ p_{21} & p_{22} & \dots & p_{2n} \\ \vdots & \vdots & & \vdots \\ p_{j1} & p_{j2} & \dots & p_{jn} \end{bmatrix} \quad (2.7)$$

The matrix p is called the proportionality constants matrix. The same approach can be used to compute the set of proportionality constants for the heating value.

There are some prerequisites that need to be fulfilled in order for Beer's law to be valid:

- 1) The incident electromagnetic radiation must consist of parallel rays travelling the same optical path length in the absorbing medium.
- 2) The incident radiation should be monochromatic or at least it should have a width narrower than absorbing transition.
- 3) The incident radiation should not cause optical saturation or optical pumping, which might give rise to stimulated emission.
- 4) The absorbing species must have a homogeneous distribution in the interaction volume and should not scatter the incident radiation.

- 5) In the case of a mixture, there should not be any interaction between the absorbers and they must act independently of each other.

In our case, all of these conditions are quite satisfied; hence, Beer's law can be used in the analysis of hydrocarbon fuel mixtures. However, at very high concentrations, when some of the particles are lying along the same optical path behind other particles, errors might be introduced. This effect is called *shadowing*. Thus, when large absorption values are to be measured, dilution is necessary in order to achieve accurate results. Measurements of absorption in the range $I/I_0 = 0.1$ to 1 are less affected by shadowing than other sources of random error. Thus, we must be sure that more than 10% of the incident light is transmitted through the sample at the absorption peaks to avoid significant errors. Other effects, such as, Rayleigh scattering by molecules, which increase at shorter wavelengths are negligible in our case.

2.2 Selection of Spectral Range

When selecting a suitable spectral region for the analysis of hydrocarbon fuel mixtures, the factors to be considered are

- 1) Spectra of pure hydrocarbon species and carbon dioxide,
- 2) The order of magnitude of absorbances at pipeline conditions and their suitability for quantitative analysis,
- 3) Variation in the spectra with pressure and temperature. In the working pressure and temperature range, the variation in the spectra with pressure and temperature should be as much systematic, preferably linear, as possible,

- 4) Spectral resolution of the sensor and sensitivity of the detector as a function of wavelength to avoid degrading sharp spectral features.

Considering the above factors, it has been shown that the near infrared region is a good choice compared to the mid infrared and far infrared. The reasons are explained below:

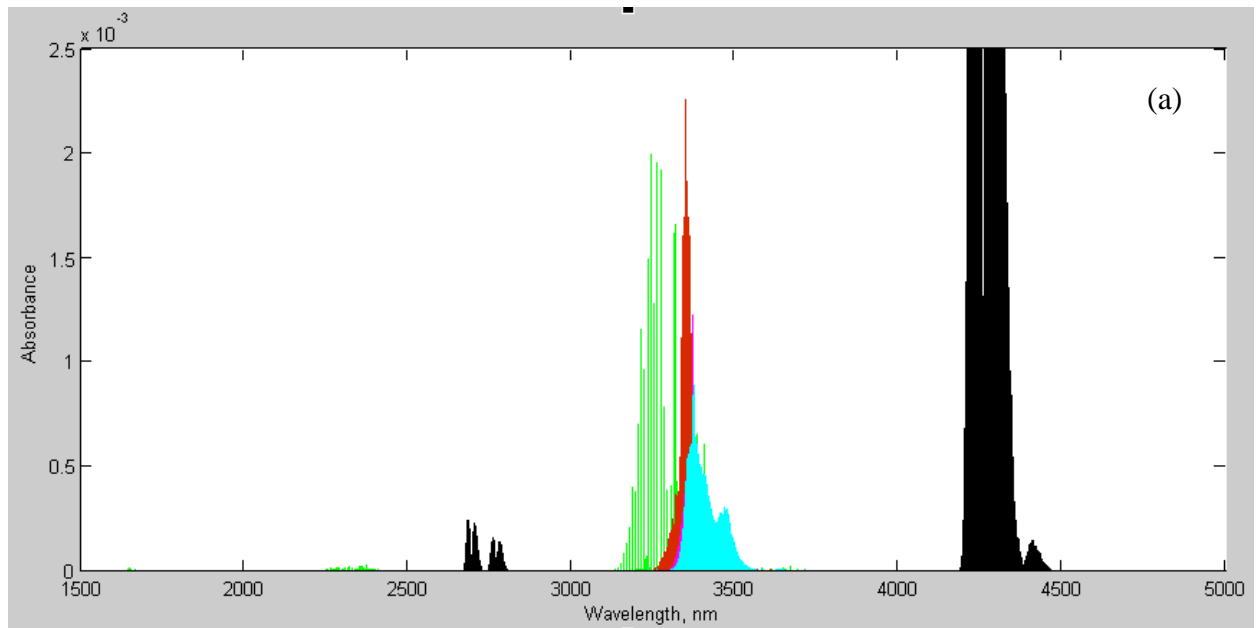
- (1) The NIR spectra of natural gas mixtures can be directly correlated to the molar concentrations of all C_1 to C_6 hydrocarbons [24] and heating value. In contrast to mid and far infrared, in the near-infrared region, absorption of hydrocarbons increases linearly with molecular density at a low spectral resolution (FWHM greater than 1 nm). The absorption spectrum of a natural gas mixture is a linear combination of the spectra of individual species [25, 26]. This eliminates the need of calibration at different pressures and/or temperatures and various compositions.
- (2) In the mid-infrared, natural gas is completely opaque at elevated pressures 6.89 bar to 68.9 bar (100 psi to 1000 psi) and pathlengths of 12.7 cm (5 inches) common for transmission lines. In the near infrared, molecular overtone and combination vibrations are forbidden by selection rules of quantum mechanics. As a result, these bands are much weaker than their parent mid-infrared bands and the molar absorptivity is quite reasonable for quantitative analysis in this region [14]. Moreover, for an average gas pressure of about 35 bar (approximately 500 psi), the absorption permits optical path lengths of about 60 cm (~ 2 feet) to be used.
- (3) According to the local mode theory [27], as the wavelength decreases, absorption becomes strongly dependent on the local CH, CH_2 , CH_3 and CH_4 bonds rather than

the molecule as a whole. As the heating value is proportional to the number and nature of these chemical bonds, heating value becomes a direct function of absorption value.

- (4) Also, NIR detectors, such as silicon-based CCDs, InGaAs, PbS devices, are less expensive compared with most MIR detectors. This is more beneficial for the purpose of commercializing the sensor.

2.3 Justification of NIR Method

Fig. 2.1 shows the IR absorbance spectra of methane, ethane, propane, butane and carbon dioxide from PNNL's Northwest-Infrared vapor phase spectral library [28]. The PNNL (Pacific Northwest National Laboratory) quantitative database is a high resolution (0.1 cm^{-1}) vapor phase infrared spectral library. These spectra are for a concentration of 1 ppm of each individual species at 296 K in 1 meter optical path length.



— Methane — Ethane — Propane — Butane — CO₂

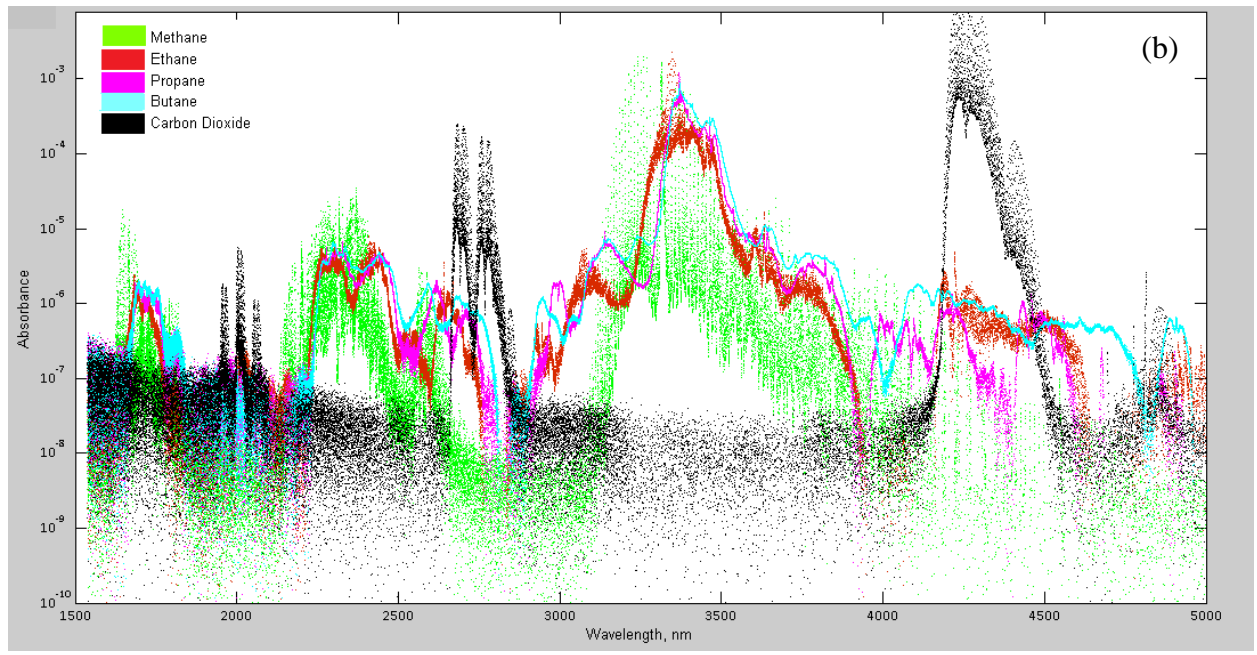


Fig. 2.1 IR absorption spectra of natural gas components (a) linear and (b) logarithmic absorbance scale [28]

The synthetic molecular absorption spectra of individual pure species – methane and carbon dioxide – were generated using the LINEPAK algorithm [29]. All the synthetic spectra are at a pressure 1.01 bar (1 atm), temperature 296 K and 30 cm optical path length; using a low spectral resolution (full width at half maximum 12.5 nm) and truncated Gaussian function for convoluting the spectra. These parameters were selected because it will be easy to calibrate the sensor at ambient conditions. At elevated pressures and/or temperatures, Beer's law can be used to predict the molar concentrations. Fig. 2.2 shows the synthetic spectra of methane and carbon dioxide in the spectral range 1000 nm to 5000 nm (11111 cm^{-1} to 2000 cm^{-1}) on linear and logarithmic scales. These synthetic spectra have been computed using spectroscopic parameters given in the HITRAN 2008 database. HITRAN stands for **H**igh-resolution **T**ransmission molecular absorption database and is a compilation of spectroscopic parameters that a variety of computer codes use to predict and simulate the transmission and emission of light.

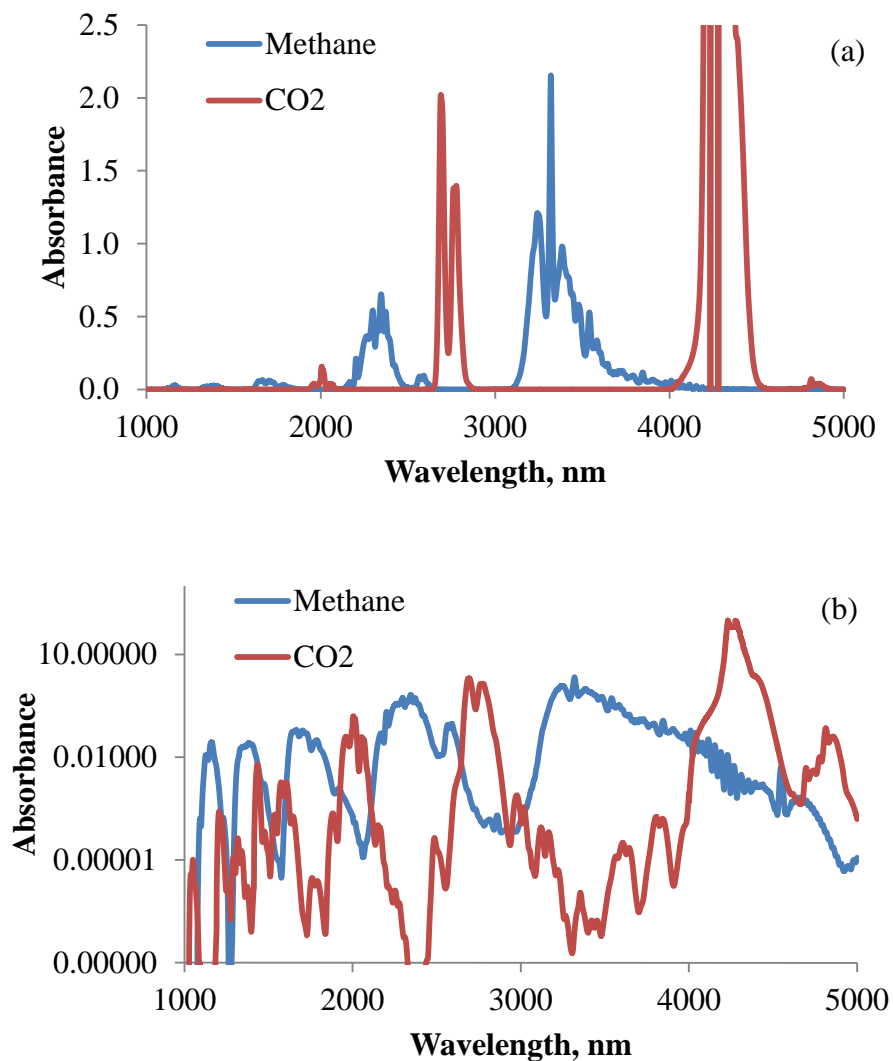


Fig. 2.2 Synthetic NIR absorption spectra of methane and carbon dioxide (a) linear (b) logarithmic absorbance scale

From Fig. 2.1 and Fig. 2.2, it is clear that hydrocarbons have adequate absorption for quantitative analysis. The absorption bands of hydrocarbons overlap with each other in almost entire region. However multivariate (multiple wavelengths) calibration techniques,

such as, principal components regression, partial least squares, can be employed to extract the desired chemical information from these spectra.

Methane has strong absorption in the mid IR. From Fig. 2.2 (a), it can be seen that the magnitude of absorbance of methane is slightly more than 2 units at ambient conditions for a path length of 30 cm. According to Beer's law, as the amount of absorption increases linearly with concentration (or density); at elevated pipeline pressures (which can be as high as 50 times the ambient pressure); the absorbance will reach a value of ~100 units. This means that natural gas mixture, which contains primarily methane, will absorb almost all the incident light at pipeline conditions in the mid infrared. Also, carbon dioxide has several interference free bands in the near infrared. These facts make NIR region near 1 micron more advantageous than MIR for hydrocarbon fuel mixture analysis.

Figure 2.3 shows the experimental absorption spectra of pure methane, ethane, propane, butane and carbon dioxide flowing at atmospheric pressure and temperature through a spectroscopic absorption cell with an effective path length of approximately 50 cm, recorded using a grating spectrometer having 12.5 nm FWHM. Figure 2.3 shows that the NIR spectra of ethane, propane and butane have very similar profile and intensities. Carbon dioxide has relatively weak absorption in NIR region.

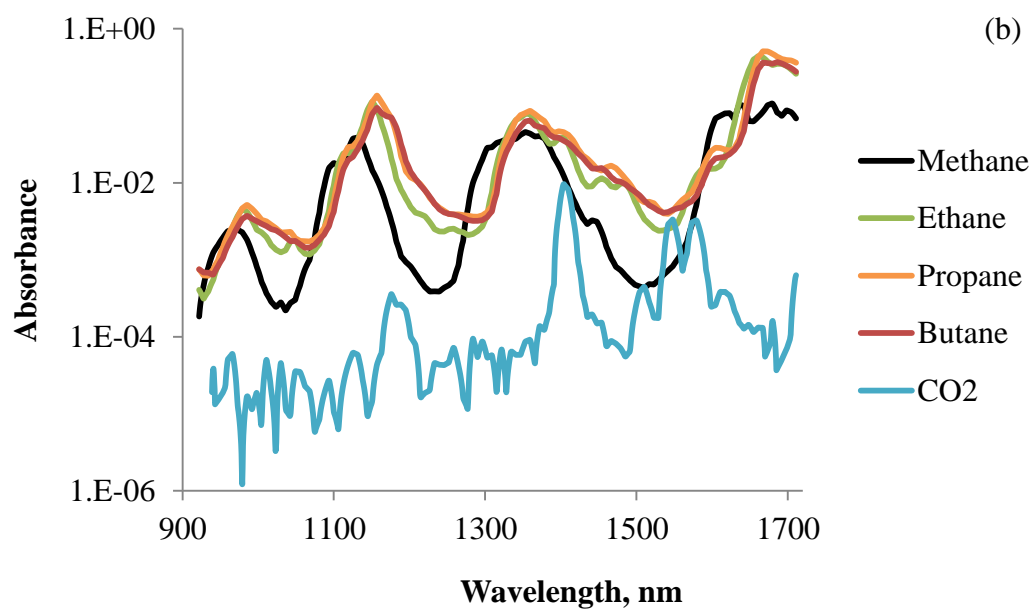
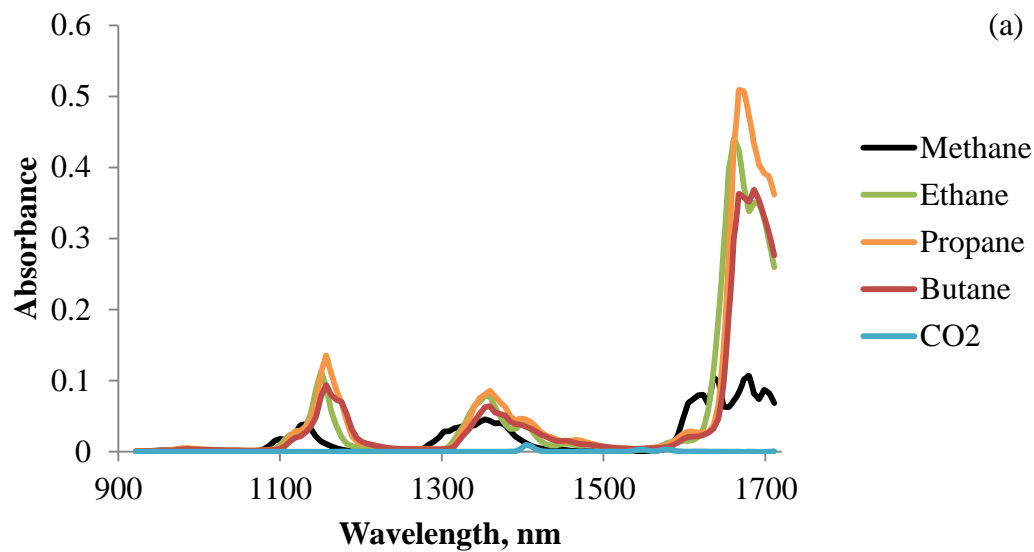


Fig. 2.3 Individual low resolution NIR spectra of C1 to C4 hydrocarbons and carbon dioxide measured in 50 cm path length at atmospheric pressure and temperature are shown with linear (above) and log (below) scales

2.4 Multivariate Analysis of Spectra

If each component were to have an interference free band, a simple formulation of Beer's law would be sufficient. However, as the peaks in a spectrum (due to different absorbers) overlap, it will not be possible to use absorbance at a single wavelength to predict the concentrations of the absorbers (called the *selectivity* problem). In such cases, it is often advantageous to combine information from several or even all spectral variables (wavelengths). The number of calibration samples available is much smaller than the number of wavelengths. The spectral measurements (concentrations and heating value in our case) are often found to have near-multicollinear relationship with wavelengths. The multivariate techniques – Principal Components Regression (PCR) and Partial Least Squares (PLS) are used to determine the regression coefficients matrix by minimizing the prediction error. In these methods, the principal components of independent variables are regressed onto the dependent variables. Typically, only a subset of the principal components is used in the regression. The principal components with the highest variance are selected for estimation. However sometimes, the principal components with low variance might also be important. The first principal component represents as much variability in the data as possible and each succeeding component as much of the remaining variability as possible. Figure 2.4 shows the model structure for PCR and PLS methods. The information in independent variable x (wavelengths) is first compressed into a few components t , where t is used as an independent variable instead of x . This variable is used in regression Eq. 2.8 with y .

$$\begin{aligned} X &= T P' + E \\ y &= T q + f \end{aligned} \tag{2.8}$$

Where X is the wavelength matrix, y is either the concentration or heating value matrix. Both X and y matrices are mean centered before they are used in the regression equations. P and q are called the loadings and they represent how the variables in T are correlated to the original variables X and y . E and f are residual matrices and represent the noise or irrelevant variability in X and y , respectively [30]. The regression coefficients calculated from Eq. 2.8 and measured absorbances of a sample test mixture, are then used to predict the concentrations of individual species and the total heating value y of the mixture. For example, if only two principal components are used, a regression model can be written as

$$y = q_0 + q_1 t_1 + q_2 t_2 + f \tag{2.9}$$

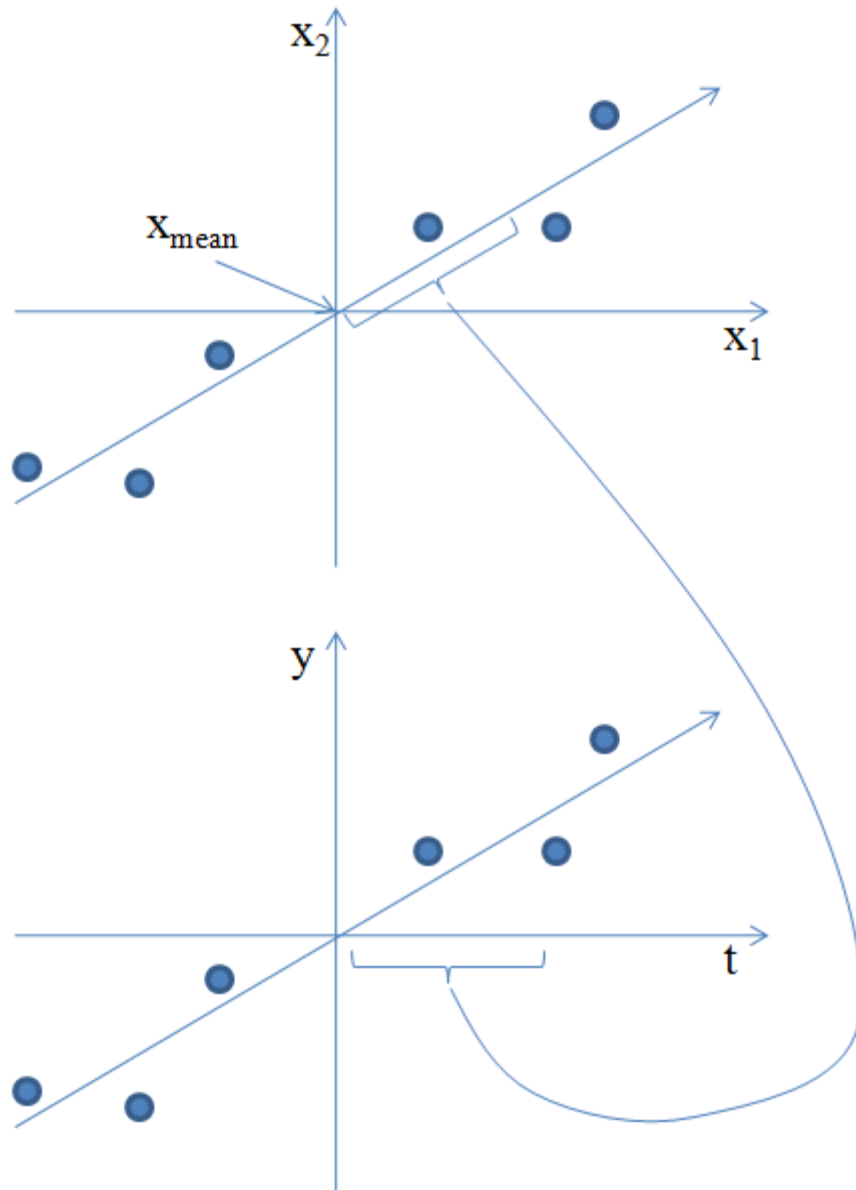


Fig. 2.4 Model structure of PCR and PLS [30]

3. EXPERIMENTAL APPROACH

3.1 Optical Setup

The basic experimental approach to absorption spectroscopy is to measure the reference intensity spectrum of the electromagnetic radiation generated by a near infrared light source with a detector and then re-measure the sample spectrum after placing a material of interest in between the source and detector. The reference spectrum and sample spectrum are affected by similar experimental conditions – spectrum of the source, absorption characteristics of other materials present in the optical path and the wavelength dependent characteristics of the detector. A dispersive element such as a diffraction grating is used to spatially disperse the radiation wavelengths into a spectrum. Fig. 3.1 shows the overall layout of experimental setup which consists of optical setup, flow control system and data acquisition system.

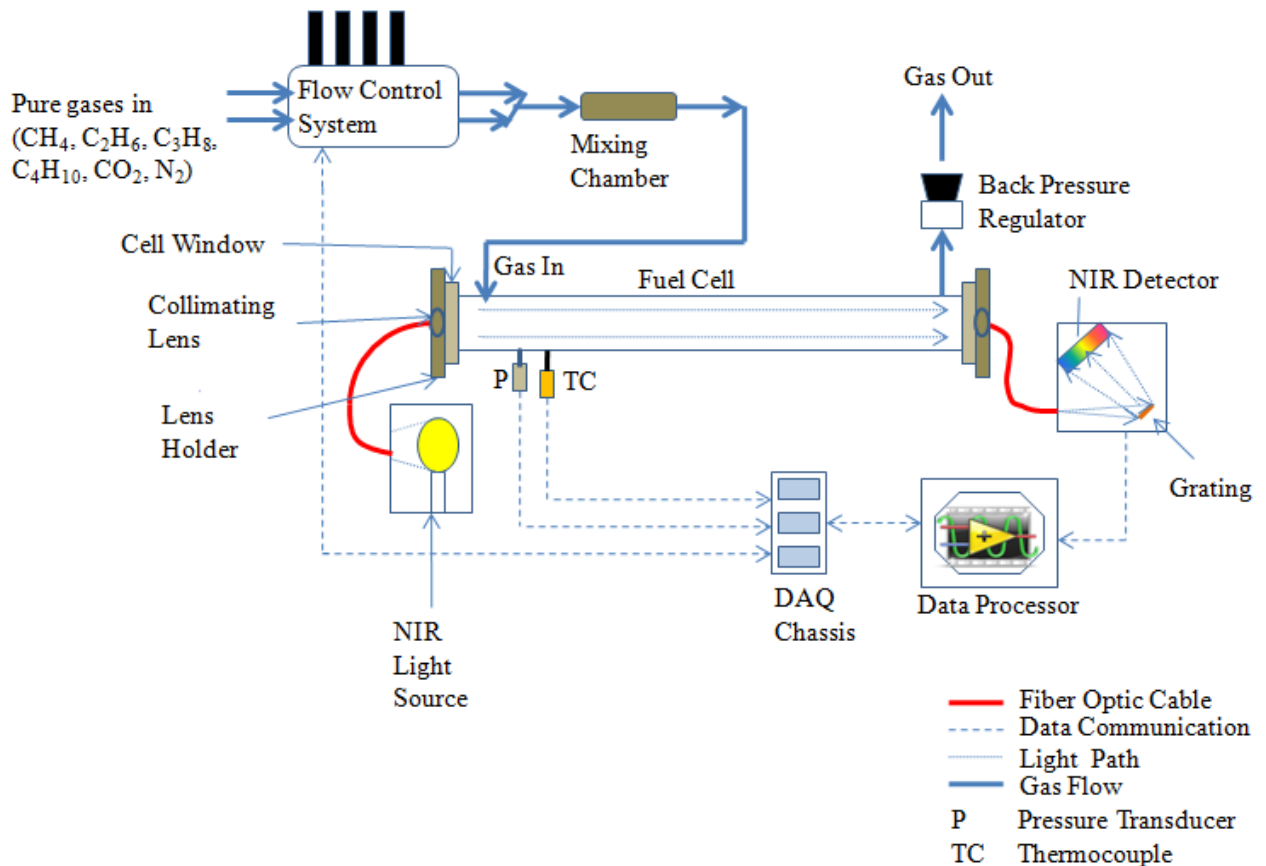


Fig. 3.1 Overall layout of experimental setup

Fig. 3.2 shows the optical setup of the gas quality sensor. The light source (LS-1-LL, Ocean Optics) is a 6.5 watts tungsten-halogen white light source, operated from a regular power supply. It has spectral output in the range 360 to 2000 nm and is connected to one end of a spectroscopic fuel cell through a fiber optic cable. The fiber optic cable, provided by Thorlabs, is a step-index, multimode, low OH fiber with 0.39 NA. The other end of the fuel cell is connected to a NIR spectrometer through another fiber optic cable. The fuel cell has an effective optical path length of approximately 30 cm, internal diameter 1.08 cm (0.426 inch),

thickness 3 mm and is made of 304L stainless steel. The path length (length of the cell) is selected so that the absorption signal is maximized at natural gas pipeline conditions to improve signal-to-noise ratio. The fiber optic cables help in minimizing the stray losses of light, as it travels from the source to the cell and from the cell to the detector. Both ends of the fuel cell are fitted with cell windows. The fuel cell and cell windows are designed to work at elevated pressures. The cell windows are fitted with lens holder, which houses collimating lenses. The collimating lenses (74-UV, Ocean Optics) convert divergent beam of light into a parallel beam. At the other end of the cell, the lens focuses the light beam onto a dispersive element through fiber optic cable. The fiber optic cable is secured to light source, collimating lenses and spectrometer through SMA905 connectors. The CDI spectrometer has 200 lines/mm grating blazed at 1315 nm. The detector is made up of InGaAs material, has 128 elements and spectral detectivity in the range 910 to 1704 nm, which results in a linear dispersion of 6.25 nm/pixel. The slit width is 50 μm . The instrumental profile has 12.5 nm FWHM (full width at half maximum).

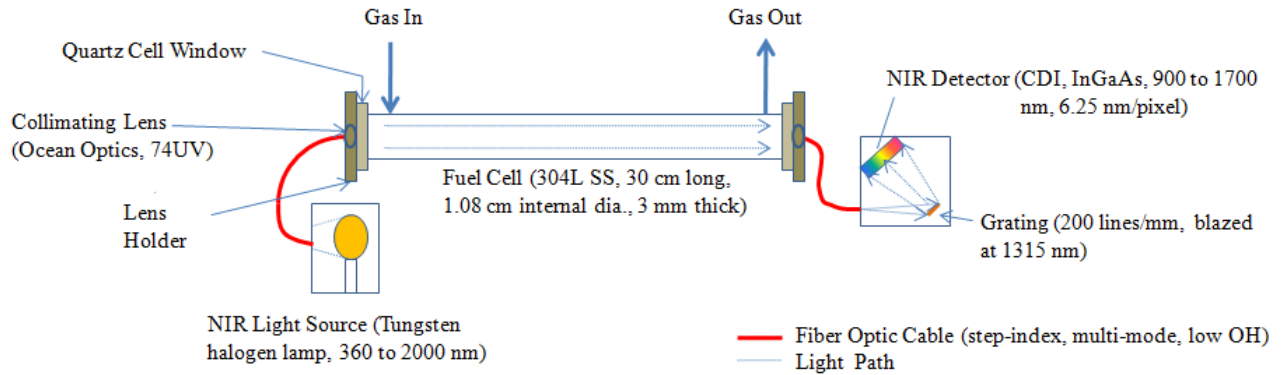


Fig. 3.2 Optical setup of gas quality sensor

3.2 Data Acquisition System

The experiment involves high-speed, real-time data acquisition from a pressure transducer, a thermocouple and the spectrometer using a software which is designed in LabVIEW using a queue-driven, state-machine-based active object. Fig. 3.3 shows the schematic of data acquisition system. The experimental parameters – pressure and temperature of the gas – are measured using the pressure transducer and a K type thermocouple and are communicated to the software through a data acquisition system configured using a National Instruments CompactDAQ9172 chassis (8-slot) and analog input modules NI9201 and NI9211 or NI9213. The pressure transducer is a Honeywell Sensotec TJE Model, bonded foil strain gage based and can read pressures up to 200 psia (~ 13.8 bar). The pressure transducer converts the measured gas pressure into 0 to 5 V output signal and communicates the signal to analog input module NI 9201. Thermocouple input module (NI 9211 or NI 9213) reads the gas temperature from the thermocouple. The spectroscopic sensor (CDI NIR128L-1.7TS) is connected to the computer directly through a USB port without any intermediate hardware.

Experimental measurements are collected in real-time; the data is processed in the GQS software and the results are displayed on the computer approximately five times every second.

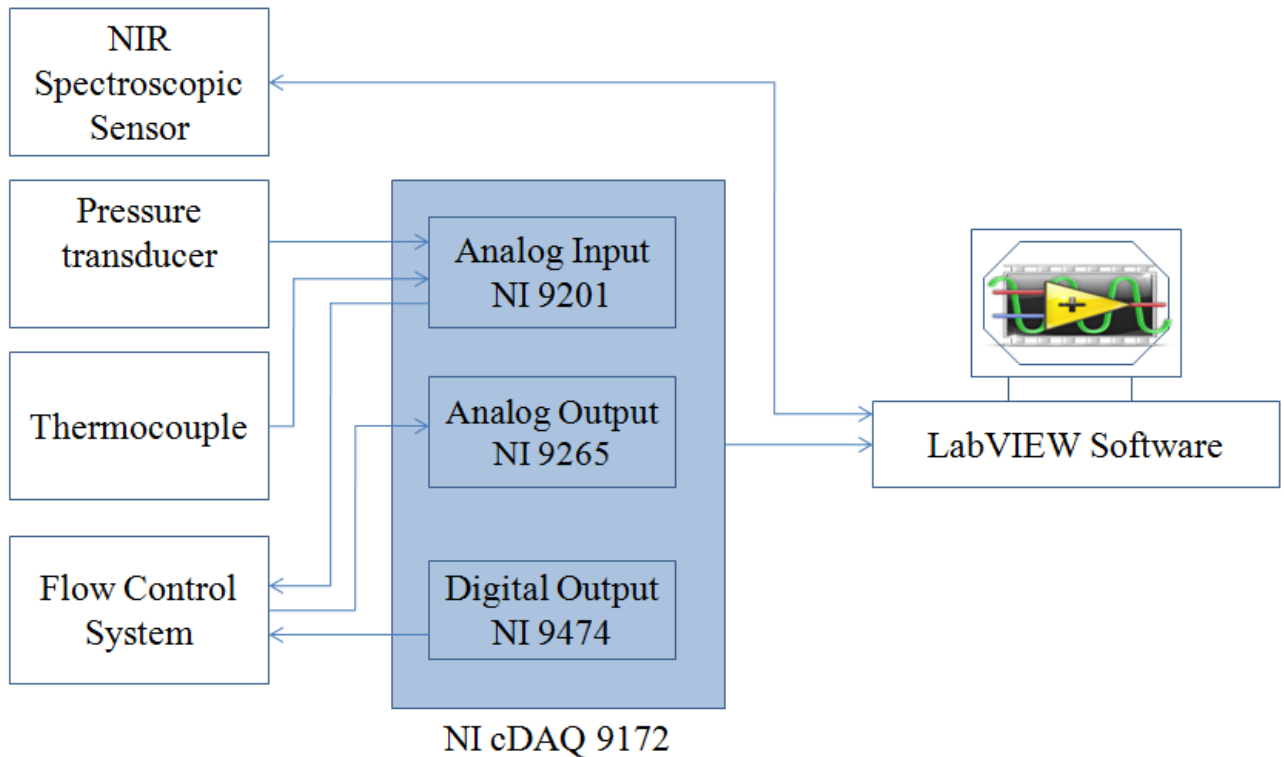


Fig. 3.3 Schematic of data acquisition system

3.3 Flow Control System

The mass flow control system is required for calibration purpose. It consists of gas supply cylinders, a mixing chamber, MKS 1179A mass flow controllers (elastomer sealed, 1000, 2000 or 5000 SCCM), National Instruments analog/digital input/output modules, MKS 247C digital channel readout and a LabVIEW application to communicate with mass flow

controllers. The gas cylinders, mass flow controllers and the fuel cell are connected by Nalgene FEP (Fluorinated Ethylene Propylene) tubing having internal diameter 3/16 inch and thickness 1/32 inch. At elevated pressures, steel tubing needs to be used. Each gas cylinder contains an individual gas (methane, ethane, propane, butane, carbon dioxide or nitrogen) and is connected to a mass flow controller. The gases flowing out of the mass flow controllers are thoroughly mixed in a mixing chamber and a homogeneous gaseous mixture flows through the fuel cell to the exhaust. Digital output module (NI 9474) turns a particular gas supply on or off. The software allows the user to manually enter the volumetric flow rate of each gas component. The mass flow controllers communicate with data acquisition chassis cDAQ9172 through the digital channel readout. The analog output module NI 9263 provides the flow setpoint signal to the mass flow controllers. The actual flow rate is computed using a feedback signal provided by each MFC to the analog input module NI 9201. The fuel cell can be purged by allowing only nitrogen to flow. Fig. 3.4 shows the connections of 4 MKS mass flow controllers to the analog/digital input/output modules.

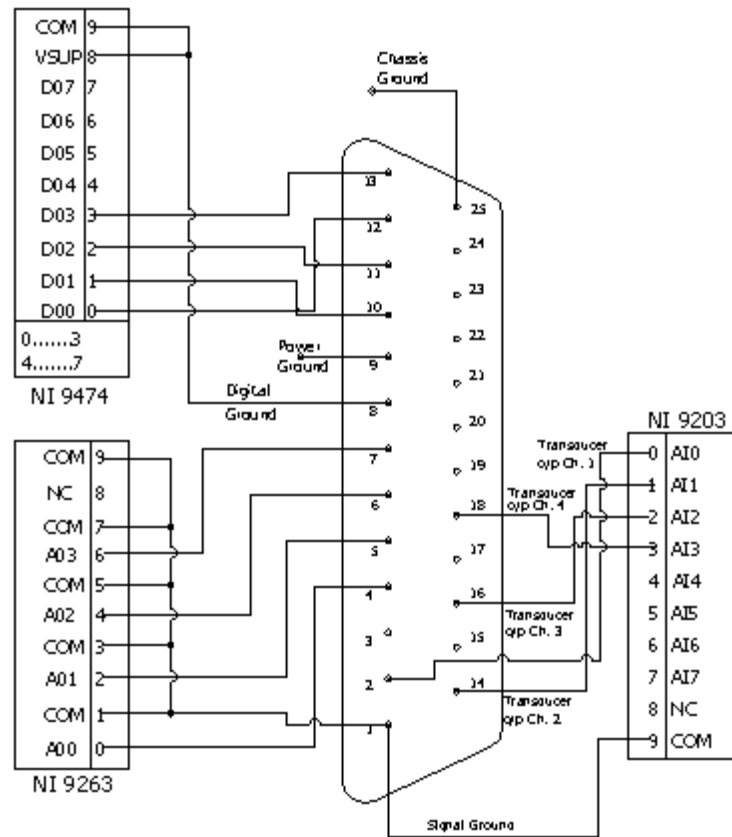


Fig. 3.4 Pin diagram for connecting flow control system to data acquisition system

3.4 Experimental Procedures

3.4.1 Spectral Calibration

For calibration, the number of sample mixtures and the composition of each mixture are determined. The quality of the resulting calibration equation depends upon the number of sample mixtures and how they were selected. The concentrations of components are selected to cover the natural range of composition variability of the mixtures to be tested. At present, we assume that the calibration and testing are to be done at the same pressure and

temperature. For example, if the measurements are to be carried out at 10 bar (~ 145 psi) and 300.15 K, we assume that calibration is also done at the same conditions.

The CDI spectrometer is connected to a computer and provides communication through Spec32 software. The Spec32 software allows capturing the background, reference intensity and transmitted intensity and allows viewing the produced spectra. Two important instrument settings in Spec32 for CDI spectrometer are integration time (seconds) and sample average. The integration time is the electronic exposure time of the detector array. The intensity level of the signal is proportional to the integration time. Integration time should be adjusted to maximize the signal without saturating the detector. The longer the integration time, the longer will be the data acquisition time and the signal to noise ratio improves. The sample average determines the number of samples that will be averaged. The signal to noise ratio increases as the square root of the number of samples averaged. The detector array has a background signal, called dark spectrum or zero light level or simply background, even when no light is incident on it. The background consists of array's thermal current and DC bias and is strongly dependent upon array's temperature and integration time. The reference intensity spectrum represents the wavelength dependent characteristics of the light source and needs to be captured before starting measurements, so that it can be divided out of the data. The reference minus the background is required to calibrate the sensitivity of each photo detector.

The light source, spectrometer, flow control system and data acquisition hardware is warmed up before starting any measurements. With the light source off, background is recorded. The spectroscopic cell is thoroughly purged with nitrogen and the reference intensity is recorded.

The volumetric flow rates of each pure gas are specified in the mass flow controller software and the gases are allowed to flow through the mixing chamber to the fuel cell. The pressures can be adjusted using a back pressure regulator connected after the gas exhaust. The pressure and temperature of the sample mixture are measured using the pressure transducer and thermocouple fixed near the gas inlet. Once the flow is established and the sample pressure in the gas cell gets stabilized, the absorption spectrum is recorded. Along with the absorption spectrum, the composition and energy content of the mixture are also stored. Before recording the spectrum, the purge gas is removed from the cell; this takes around 20 seconds after the sample mixture flow starts. The pressure in the cell should be the same for purging gas and sample mixture to minimize errors in measurements due to static pressure effects in the absorption cell and other effects like refraction which is a function of pressure for gases. The procedure is repeated and spectra are recorded for all calibration mixtures in a database. The background and reference intensities are re-acquired before taking the spectrum of each sample mixture. Once all the data is collected, using the PCR and PLS calibration methods, regression coefficients for composition and heating value are computed.

3.4.2 Validation

The prediction testing procedure is essentially the same as calibration, except the fact that, in prediction testing, the set and predicted properties are compared and a graph of prediction error versus the number of scores (components) is plotted for each property and calibration method. The numbers of scores corresponding to the minimum prediction error are selected and the same numbers of scores are used during actual field measurements.

3.5 Analysis of the Experimental Error

In this experiment, the potential sources of errors in spectral measurements are as follows:

- 1) Flow control system: It is very difficult to achieve the desired volumetric flow rate exactly. The actual flow rate will always deviate slightly from the set flow rate, due to inaccuracy of the mass flow controllers.
- 2) The sample pressure should be as close to the purging gas (nitrogen) pressure as possible to minimize measurement errors due to effects like scattering, reflection etc.
- 3) Optical instabilities, such as variation of light source temperature and intensity, background noise and detector sensitivity drift might introduce a large error in the absorbance. This error can be minimized by recording the background and reference intensities periodically.
- 4) The principal components (or scores) with the highest variance should be selected so that they represent as much variability in the data as possible.

In order to determine the accuracy of the predicted results, the difference between each set and predicted value (concentration of each individual component and the total heating value) are calculated. These differences are called residuals. The root mean squared error is defined by Eq. 3.1 and represents a single measure of predictive power.

$$RMSE = \left[\frac{\sum (E_{set} - E_{predicted})^2}{m} \right]^{1/2} \quad (3.1)$$

Where E_{set} and $E_{predicted}$ are the set and predicted energy content of m samples used for testing. In a similar way, the error can be calculated for the predicted concentration of each individual component.

For validation, it is useful to plot the set and predicted values. The predicted values should be close to a 45° straight line as shown in Fig. 3.5. From the plot, we can also identify the regions with different levels of prediction accuracy. Generally, measured y values, lower than the average, are overestimated, while y values, above than average, are underestimated. This is due to the least squares effect. In order to minimize prediction errors, the optimal number of scores A corresponding to the minimum prediction error should be used for measurements. For each calibration method used, prediction error is plotted against the number of scores for each predicted concentration and the total heating value. From these graphs, the number of scores to be used is determined. Typically, the prediction error is large for small values of the number of components, decreases as the number of components increases and increases as the number of components becomes too large.

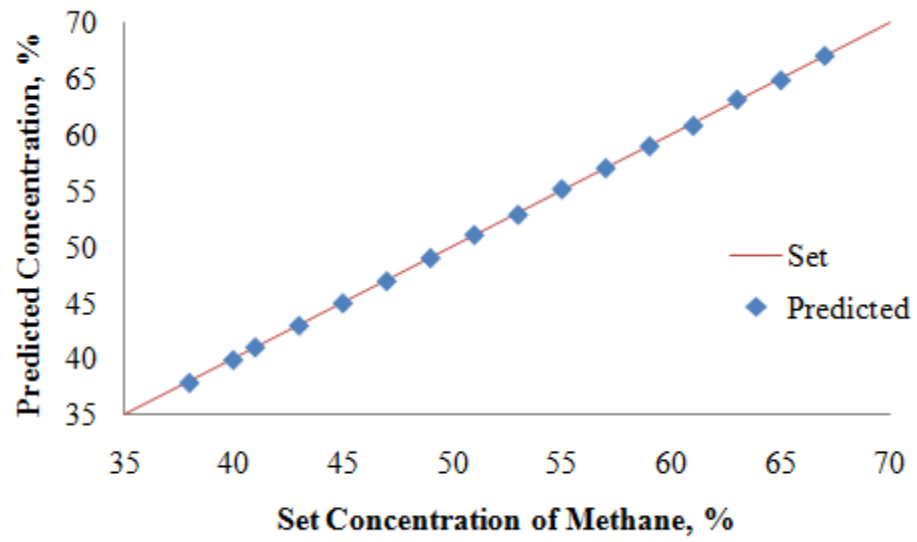


Fig. 3.5 Example of a typical prediction testing result

4. LINEARITY OF NIR SPECTRA OF HYDROCARBONS

4.1 Spectral Line Broadening and Shift

A spectral line extends over a range of frequencies, not a single frequency. In addition its center may be shifted from its central wavelength. The reasons for this broadening and shift may be either local or non-local conditions as described below.

1. *Natural line broadening*: The lifetime of an excited state is finite due to the spontaneous decay of emitted radiation. The shape of the broadened line is determined by the three-parameter probability density function of the Lorentzian form,

$$I(\nu) = \frac{I(\nu_0)}{1 + [(\nu - \nu_0)2\pi\tau]^2} \quad (4.1)$$

where I is the intensity at a frequency ν and ν_0 is the line center. The full width at a half maximum (FWHM) is,

$$\begin{aligned} \Delta\nu_{1/2} &= 1/\pi\tau. \\ \frac{\Delta\nu_{1/2}}{\nu} &= \frac{\Delta\lambda_{1/2}}{\lambda} \\ \Delta\lambda_{1/2} &= \frac{\Delta\nu_{1/2}}{\nu} \lambda = \frac{\lambda}{\pi\tau\nu} = \frac{\lambda^2}{\pi\tau c} \end{aligned} \quad (4.2)$$

The lifetime of emission is of the order of 10^{-8} seconds. Let's find the out the order of magnitude of the FWHM at a wavelength of 1 μm ,

$$\Delta\lambda_{1/2} = \frac{(1 \times 10^{-6})^2}{\frac{22}{7} \times 10^{-8} \times 3 \times 10^8} \sim 10^{-13} \text{ m} = 10^{-4} \text{ nm}$$

2. *Thermal Doppler broadening*: This arises due to the Doppler shift caused by the thermal motion of molecules.

$$\Delta v = v - v_0 = v_0 v/c$$

Here v is the particle velocity. The higher is the temperature of the gas, the wider will be the distribution of velocities in the gas and hence the broader the spectral line. Broadened line has a Gaussian profile which describes Maxwellian velocity distribution and there is no associated shift.

$$I(v) = I(v_0) \exp \left[\frac{-(v - v_0)^2 c^2}{2V_{ta}^2 v_0^2} \right] \quad (4.3)$$

Where $V_{ta}^2 = T_a / m_a$. The subscript 'a' refers to the emitting atom. The full width at half maximum is

$$\Delta v_{1/2} = v_0 \left(\frac{v_{ta}}{c} \right) (2 \ln 2)^{1/2} \quad (4.4)$$

Let's find out the order of magnitude of the full width at half maximum at $T = 300.15$ K and $\lambda_0 = 1 \mu\text{m}$ for a hydrogen atom ($m_a = 1.674 \times 10^{-27}$ kg).

$$\begin{aligned} \Delta \lambda &= \sqrt{\frac{8kT \ln 2}{mc^2}} \lambda_0 = \sqrt{\frac{8 \times 1.3806503 \times 10^{-23} \times 300.15 \times \ln 2}{1.674 \times 10^{-27} \times (3 \times 10^8)^2}} \times 10^{-6} \\ &= 1.235 \times 10^{-11} \text{ m} = 0.012 \text{ nm} \end{aligned}$$

3. *Pressure broadening*: This effect arises due to the presence of nearby particles and their effect on the emitted radiation.

a) *Impact pressure broadening*: The collision of other particles with emitting particle interrupts the wave train. The duration of collision is much shorter than the lifetime of the emission process. This effect depends on both the density and temperature of the gas. This broadening effect is described by a Lorentzian profile and there may be an associated shift.

$$\Delta\nu \sim \frac{1}{\tau}$$

$$\Delta\lambda_{1/2} = \frac{\Delta\nu_{1/2}}{\nu} \lambda = \frac{\lambda}{\tau\nu} = \frac{\lambda^2}{\tau c}$$

At $\lambda = 1 \mu\text{m}$,

$$\Delta\lambda_{1/2} = \frac{u}{l^*} \frac{\lambda^2}{c} \quad (4.5)$$

Where u is the velocity of molecules and l^* is the mean free path. According to the kinetic theory, if the velocities of identical particles have a Maxwell distribution of velocities, the following relationship applies

$$l = \frac{k_B T}{\sqrt{2} \pi d^2 p} \quad (4.6)$$

Where k_B is the Boltzmann constant, T is the temperature, p is the pressure and d is the diameter of the gas particles. At ambient pressure and temperature conditions, the mean free path is found to be approximately 68 nm.

$$\Delta\lambda_{1/2} = \frac{343}{68 \times 10^{-9}} \frac{(1 \times 10^{-6})^2}{3 \times 10^8} = 1.68 \times 10^{-11} \text{ m} = 0.0168 \text{ nm}$$

b) *Quasistatic pressure broadening*: In quasistatic approach, an atom is assumed to radiate in an environment that is effectively static during the period of emission. The presence of other

particles shifts the energy levels in the emitting particles, thereby altering the frequency of the emitted radiation. The duration of this influence is much longer than the lifetime of the emission process. This effect is primarily caused by the density of the gas and is rather independent of the temperature. There may be an associated shift as well.

Combinations of broadening effects: Sometimes Doppler and other broadening effects, finite resolution of the measuring instrument are important. These mechanisms can act in isolation or in combination with others. If we assume that the effects are independent of each other, the resulting line profile is a convolution of individual line profiles.

$$f(\Delta\nu) = \int f_1(\Delta\nu - \Delta\nu') f_2(\Delta\nu') d(\Delta\nu') \quad (4.7)$$

For example, a combination of thermal Doppler broadening and impact pressure broadening results in Voigt profile. For Gaussian line shape, the convolution of two profiles of width Δ_1 and Δ_2 , the final width is given by

$$\Delta^2 = \Delta_1^2 + \Delta_2^2 \quad (4.8)$$

While for a Lorentzian shape

$$\Delta = \Delta_1 + \Delta_2 \quad (4.9)$$

In both the cases, the convolved profile is a profile of the same form, Gaussian or Lorentzian. It should be noted that the individual line broadening mechanisms are not always independent of each other. For example, the impact pressure broadening and thermal Doppler broadening can act in a coherent manner to narrow the line profile, called Dicke effect. The combination of peak width broadening due to lifetime, pressure and temperature are often

narrow to be observed with a particular spectrometer. In this case, the instrument function dominates.

4.2 NIR Spectra of Hydrocarbons and Carbon Dioxide at Elevated Pressures

Natural gas is transported over long distances through pipelines having diameters depending upon the pipeline. Table 4 gives the diameter ranges in various pipelines.

Table 4. Natural gas pipeline diameters [31].

Type of pipeline	Diameter (inches)
Main pipeline	16 to 48
Interstate	24 to 36
Lateral	6 to 16
Local delivery	0.5 to 3

Compressor stations, located every 100 to 245 miles, pump the gas at 14 to 100 bar (~ 200 to 1500 psi). The local delivery pipelines may have pressures as low as 0.2 bar (3 psi), while the main pipelines may have pressures up to 100 bar [31]. The pressure in the pipelines changes with changing pipe diameter, due to pressure drop with distance along the length of the pipe, friction loss, height change etc. Although, the temperature drops due to drop in pressure, the temperature can be assumed to be constant, as the flowing gas gains some heat from the environment. It will be easy to calibrate the sensor at atmospheric conditions and use this calibration database to perform the measurements at pipeline pressures. If the density

variations are taken into account while processing the spectral data, there is no need to monitor the pressure or temperature in the fuel cell during calibration or measurements.

It becomes necessary to study the spectral effects associated with pressure and temperature broadening of spectral lines and associated shift in the line centers of hydrocarbons in NIR region. Considering the working range of pressure and temperature, in our case, it is anticipated that the pressure broadening will always dominate the thermal Doppler broadening. The NIR absorption spectra of three pure species – methane, propane and carbon dioxide – were recorded in the pressure ranges 1 to 13.65 bar (14.5 to 198 psi) for methane, 1 to 8.2 bar (14.5 to 119 psi) for propane and 1 to 3.5 bar (14.5 to 50 psi) for carbon dioxide. The pressure ranges were determined considering the maximum mole fractions of these gases in a natural gas mixture. High purity nitrogen (99.998%) and CP grade methane (99.0%) are used in the experiment. Each gas cylinder is connected to the absorption cell by Swagelok steel tubing, which is designed to work at elevated pressures and temperatures. A three-way valve can be used to switch the flow between gases. The gas is introduced in the fuel cell. Effects, such as, scattering, transmission of light outside the cell, are negligible. It is assumed that there are no thermal gradients in the gas, hence no turbulence from thermal gradients. The temperature of the gas is measured using a K-type thermocouple kept at the gas inlet. The full scale value of the pressure transducer was 200 psi (~ 13.8 bar, 0.1% accuracy). The pressure in the cell was kept stable using a back pressure regulator (0 to 1000 psig) connected after the exhaust. The back pressure regulator is followed by a rotameter to control the flow rate. Accuracy of the mass flow controllers for calibration gas was $\pm 1\%$ of reading (20 to

100% of full scale). The pressure in the cell remained stable to within 2.75% of the set pressure or better. The main causes for instability in the gas pressure are fluctuations in the flow rate due to inaccuracy of the mass flow controllers and back pressure regulator. All the spectra were recorded consecutively on the same day. Typically, 100 scans were averaged for measuring reference and sample intensities. At each pre-determined pressure setpoint, the reference intensity $I_0(\lambda)$ and sample intensity $I(\lambda)$ were recorded. However, the background was acquired only once before starting the measurements. Absorption spectra were obtained by dividing the sample spectra by the spectra obtained for nitrogen (as explained in *Chapter 2*, nitrogen is a homonuclear diatomic molecule and is spectrally inactive in NIR). Table 5 gives an overview of measurement conditions applied in this study. According to Beer's law, the absorbance depends upon the molecular density. Thus, it is important to study the variation of absorbance with density, rather than pressure or temperature. Fig. 4.1 shows the variation of density with pressure for methane, propane and carbon dioxide at a temperature of 296.65 K (measured during experiment). The compressibility factors are calculated using the three parameter principle of corresponding states and the values of $Z^{(0)}$ and $Z^{(1)}$ are read from Lee-Kesler tables. In the considered pressure range, the compressibility factors of these gases are very close to 1 and as a result, the density of each gas increases almost linearly with its pressure. Fig. 4.2 shows the absorption spectra of methane, propane and carbon dioxide measured at elevated pressures.

Table 5. Laboratory measurement conditions.

Flow rate	2.2 SCFH of air
Temperature	296.65 K
Integration time	0.01 seconds
Number of scans	100
Instrument width (FWHM)	12.5 nm

	P, psi	P, bar	Z	$\rho=P/ZRT$
CH₄	14.4	0.9928	0.9983	0.6468
	24.7	1.7030	0.9970	1.1108
	50.0	3.4474	0.9940	2.2554
	75.0	5.1711	0.9910	3.3932
	100.5	6.9292	0.9880	4.5609
	124.0	8.5495	0.9852	5.6434
	150.5	10.3766	0.9820	6.8714
	174.0	11.9969	0.9793	7.9670
	198.0	13.6516	0.9764	9.0923
	217.6	15.0000	0.9741	10.0141
C₃H₈	14.4	0.9928	0.9831	1.8052
	19.5	1.3445	0.9771	2.4597
	40.5	2.7924	0.9516	5.2455
	60.0	4.1369	0.9269	7.9777
	80.4	5.5434	0.8984	11.0296
	100.0	6.8948	0.8706	14.1565
	119.0	8.2048	0.8437	17.3844
	217.6	15.0000	0.2445	109.6678
CO₂	14.5	0.9997	0.9947	1.8021
	20.0	1.3790	0.9927	2.4907
	25.0	1.7237	0.9908	3.1191
	30.5	2.1029	0.9888	3.8131
	35.6	2.4518	0.9870	4.4540
	40.2	2.7717	0.9853	5.0439
	45.2	3.1164	0.9834	5.6818
	50.4	3.4736	0.9815	6.3452
	217.6	15.0000	0.9180	29.2957

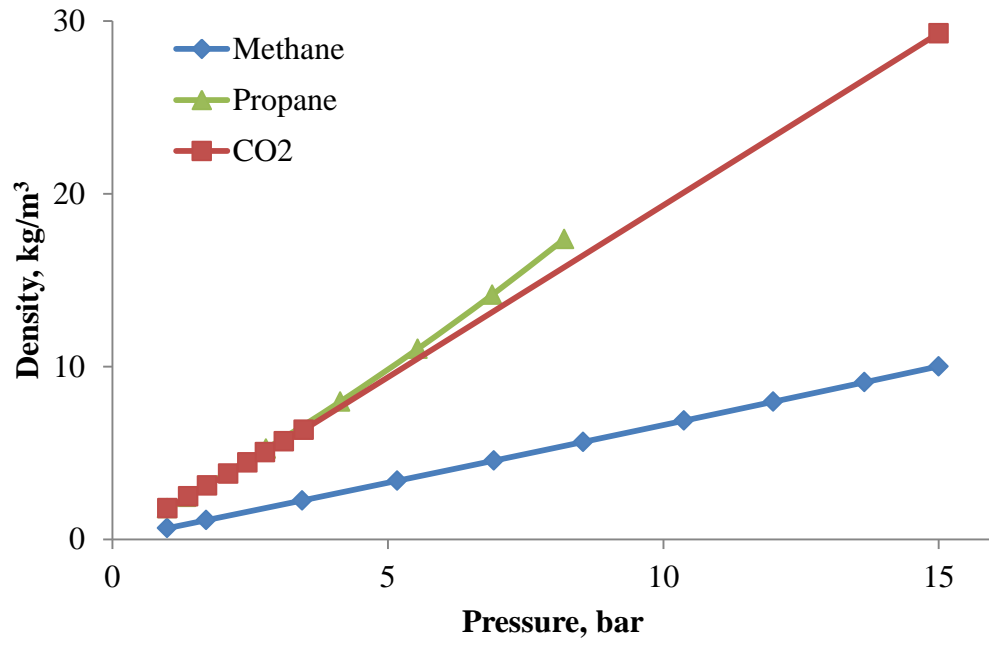


Fig. 4.1 Linearity in the density with pressure ($Z \sim 1$)

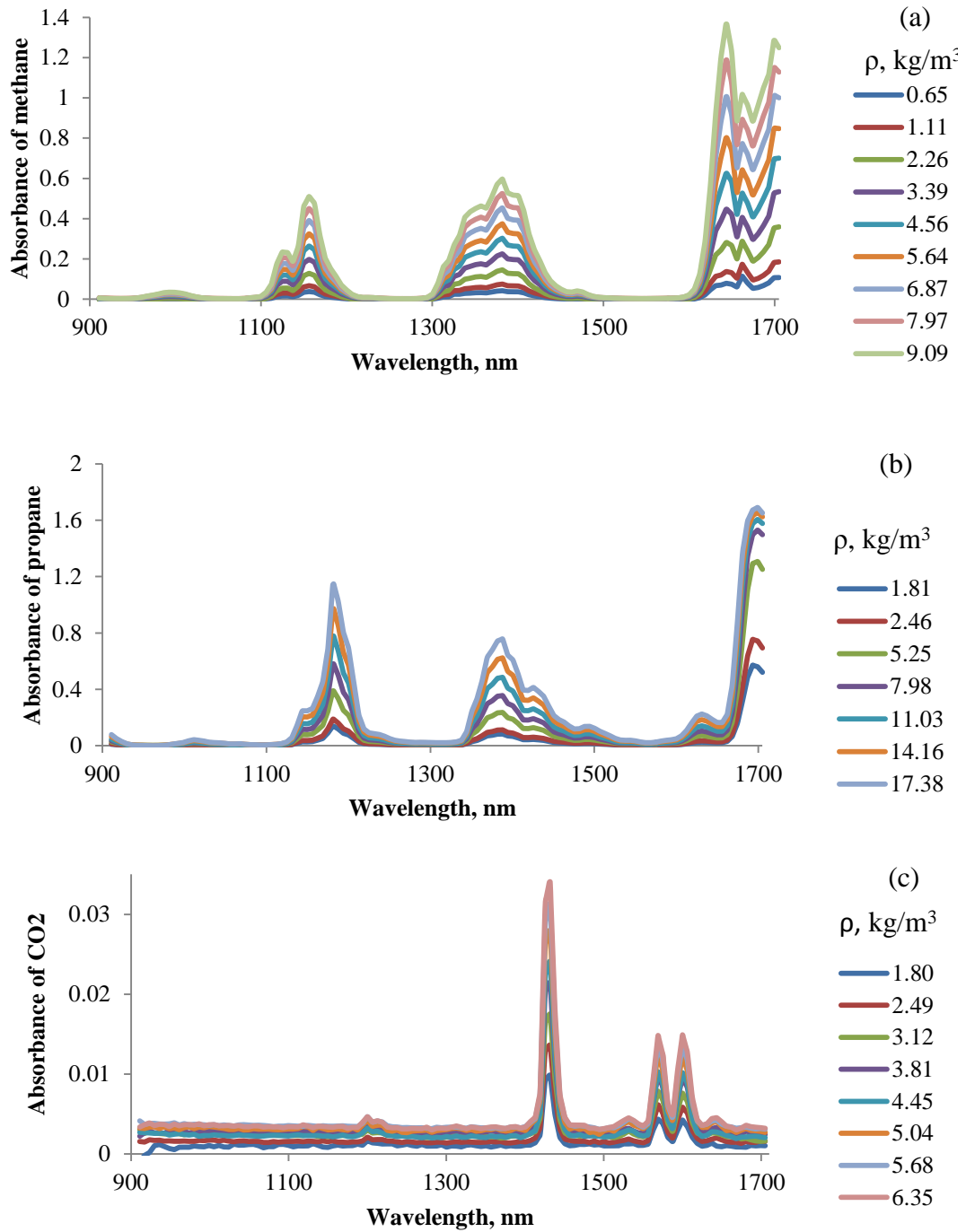


Fig. 4.2 NIR absorption spectra at elevated pressures for (a) methane (b) propane (c) carbon dioxide

4.3 Results and Discussion

It is clear from Fig. 4.2 that the spectroscopic sensor undersamples the spectra relative to their resolution, but it appears to be satisfactory for obtaining an overview of the band shape/profiles and integrated band intensities. As a trade-off to broad spectral coverage, spectral band features are recorded with low spectral resolution and/or inadequately fine detector binning. The measured physical spectrum is affected by instrumental performance. As the line width observable with the instrument is greater than the natural line widths, the individual vibrational and rotational lines in the spectrum appear clustered together in bands. The absorption bands of alkanes in this region are all overtones and combinations of the fundamental vibrational modes. Methane spectrum consists of discrete absorption bands of decreasing intensity at shorter wavelengths. The four fundamental vibrations of methane are: symmetric and asymmetric stretches, $\nu_1 = 3431.71 \text{ nm}$ (2914 cm^{-1}) and $\nu_3 = 3311.26 \text{ nm}$ (3020 cm^{-1}); two bending modes, $\nu_2 = 6563.08 \text{ nm}$ (1526 cm^{-1}), $\nu_4 = 7656.97 \text{ nm}$ (1306 cm^{-1}). Only the ν_3 and ν_4 are infrared active [32]. The band assignments in the studied region can be made as two-stretch, two-stretch + bend and three-stretch in the order of decreasing wavelength (or decreasing intensity) [33]. From Fig. 4.2, we cannot easily see the effect of spectral line broadening in this figure, as the pressure range is quite small. However, as we go to higher pressures, the spectral valleys will become filled in. The primary spectral effect is the increase in absorption signal with increasing pressure. The overall band shape/profile shows a systematic change with pressure over this range. We will focus on each absorption band for a more detailed analysis. The absorption bands can be roughly identified in the following ranges – 1100 to 1200 nm, 1300 to 1500 nm and 1600 to 1700 nm for methane;

1120 to 1220 nm, 1330 to 1570 nm and 1580 to 1650 nm for propane; 1400 to 1450 nm and 1525 to 1650 nm for carbon dioxide. For propane, 1580 to 1650 nm range is selected instead of 1580 to 1700 nm, because at pressures greater than 5.5 bar (80 psi), the absorption of propane reaches a value where the output of the light source, used in the experiment, becomes inadequate. Fig. 4.3 shows that the average absorbance scales with density over the wavelength range considered. Average absorbance represents the area under an absorption band.

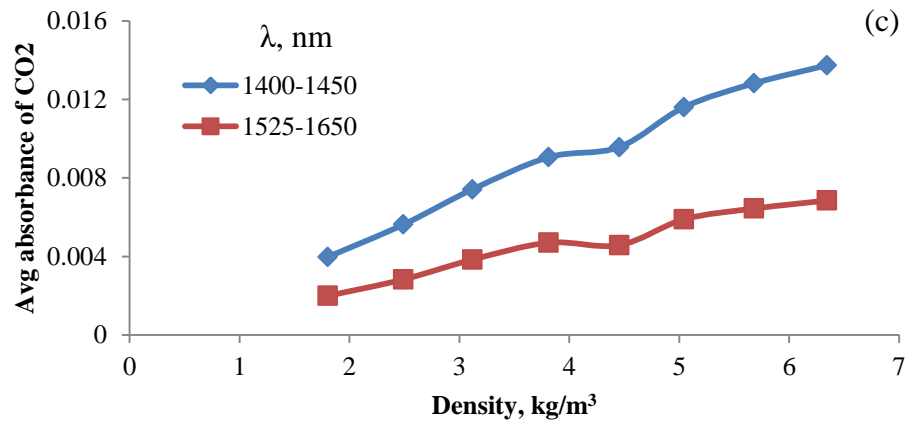
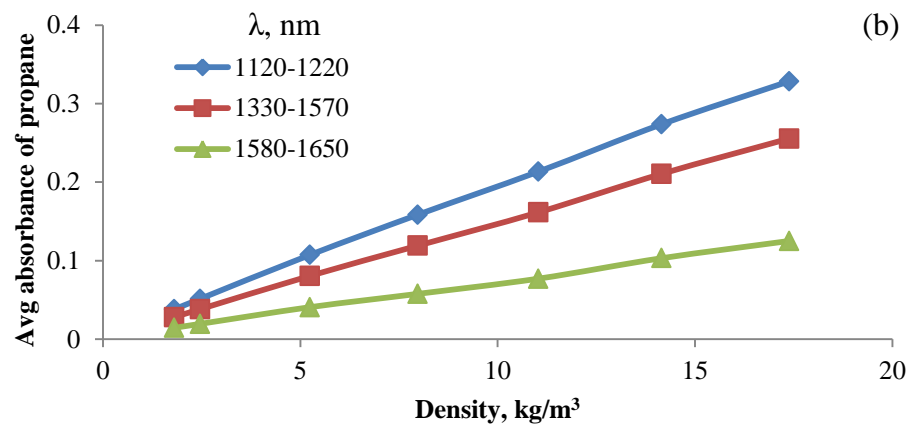
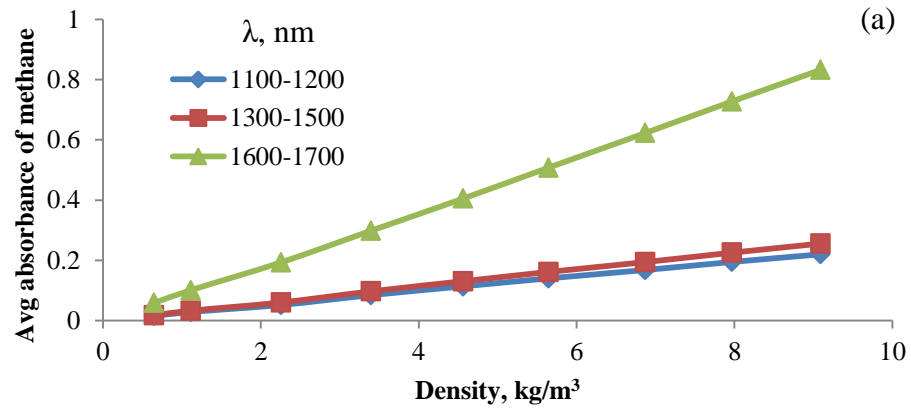


Fig. 4.3 Linearity of NIR absorption with density for (a) methane (b) propane and (c) carbon dioxide

Fig. 4.3 shows an excellent fit of data to a straight line with its intercept at the origin. Similarly, Fig. 4.4 shows an excellent linear fit between the absorbance and density at wavelengths selected from each absorption band. This linearity has also been found to be true with increasing temperatures [25]. Thus, the peak area and absorbance vary largely with density, rather than separately with pressure or temperature and hence, we can conclude that NIR absorption of methane, propane and carbon dioxide increases linearly with density. The NIR spectra of n-heptane are linear with density [25]. Thus, for hydrocarbons and carbon dioxide, the NIR region near 1 μm is ideal and is very easy to use over the desired range of pressure and temperature in industrial applications.

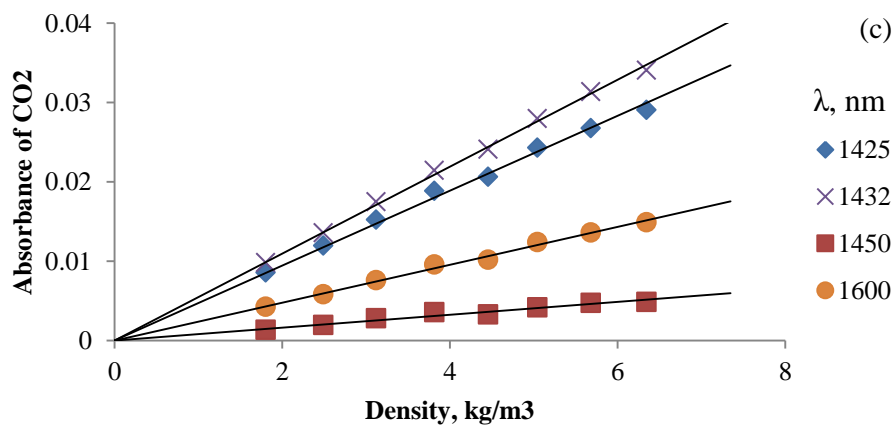
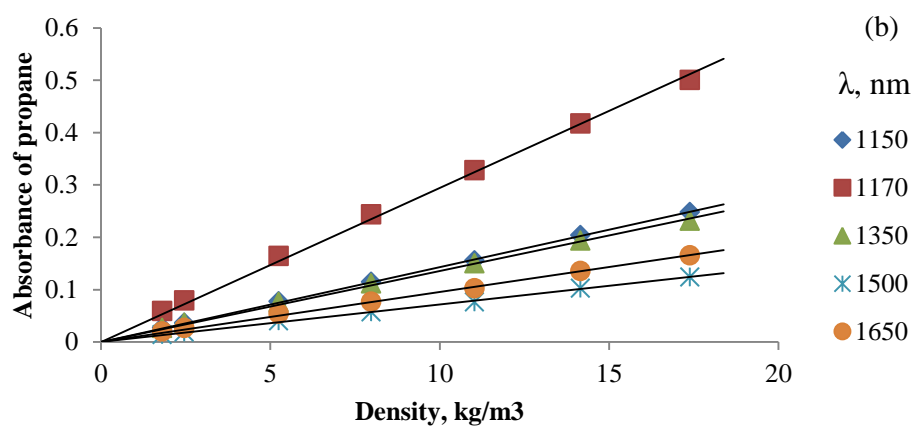
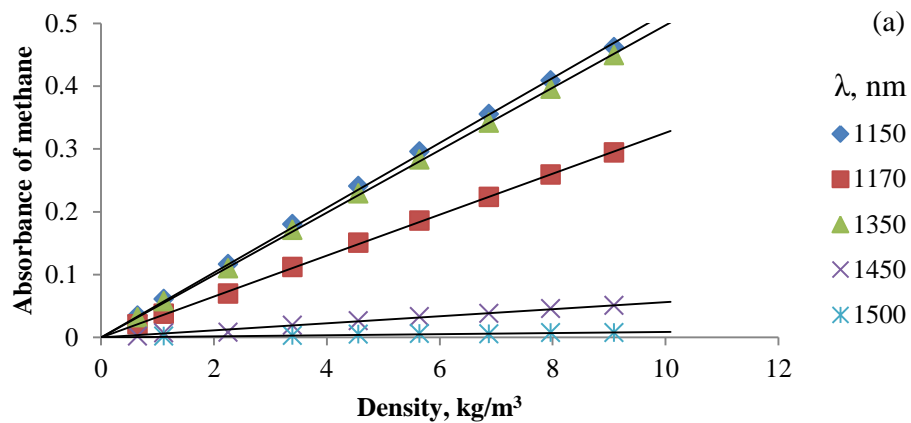


Fig. 4.4 Linearity in absorbance with density at selected wavelengths for (a) methane (b) propane and (c) carbon dioxide

Suppose P_0 , T_0 , ρ_0 are the pressure, temperature and density of a pure gas at laboratory conditions and $A_0(\lambda)$ is the absorbance measured at a wavelength λ , where λ lies in the near infrared region (in our case, $900 \leq \lambda \leq 1700$). Now, if a spectral measurement $A(\lambda)$ is recorded at another set of conditions P , T and ρ ; the two measurements can be mathematically correlated using the linearity between absorbance and density without much loss of accuracy [Eq. 4.10].

$$A_0(\lambda) = A(\lambda) \times \frac{\rho_0}{\rho} = A(\lambda) \times \frac{P_0}{Z_0 T_0} \times \frac{Z T}{P} = A(\lambda) \times \frac{P_0}{P} \times \frac{T}{T_0} \times \frac{Z}{Z_0} \quad (4.10)$$

Fig. 4.5 shows the NIR spectra, measured at elevated pressures, scaled down to the ambient pressure (~ 1 bar) using Eq. (4.10) ($T=T_0$ for laboratory measurements). From Fig. 4.5, it can be easily seen that all the density corrected absorbance spectra overlap quite well with each other.

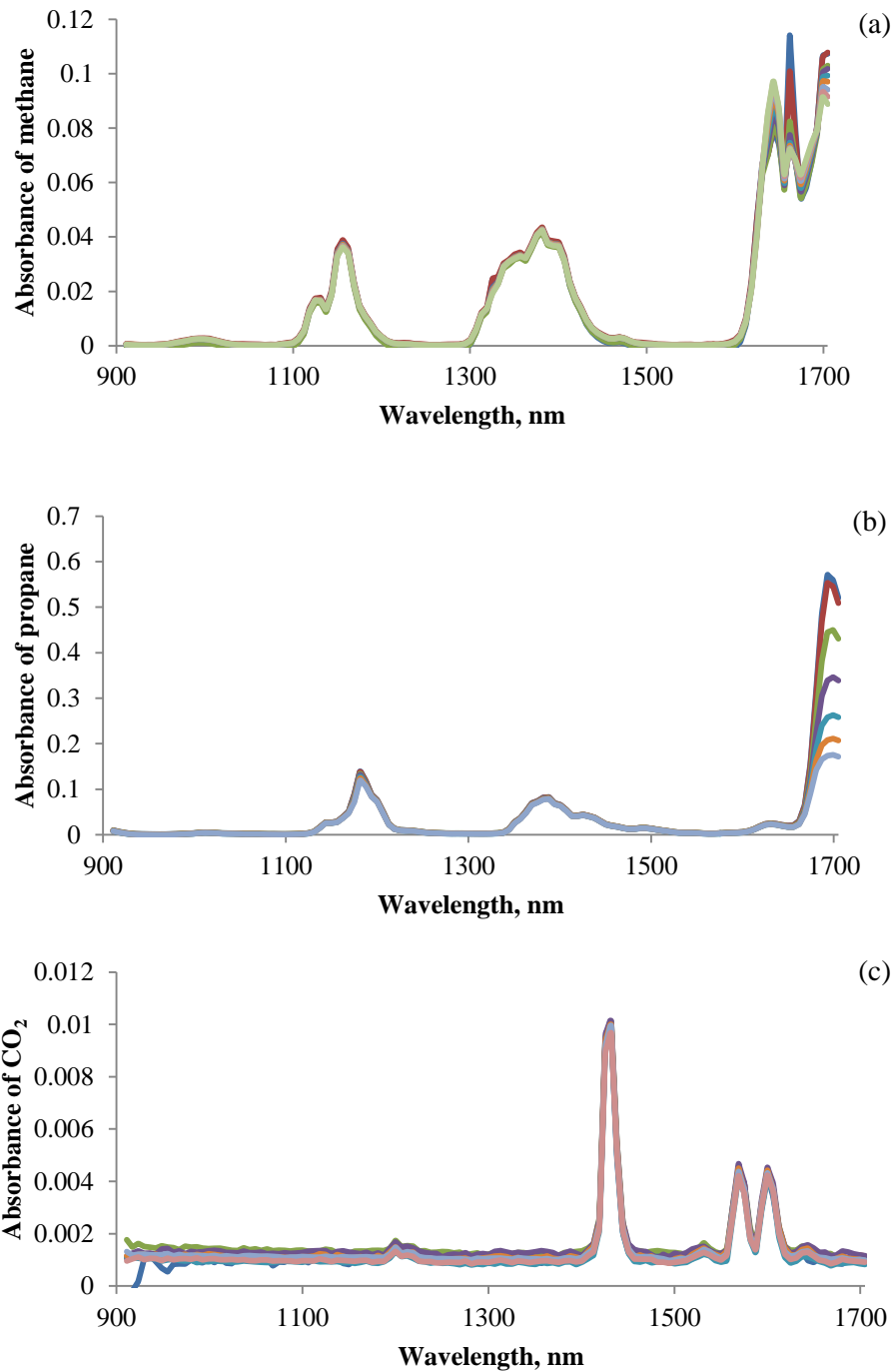


Fig. 4.5 NIR spectra scaled down to ambient pressure for (a) methane (b) propane and (c) carbon dioxide

4.4 Correcting the NIR Spectra for STP Conditions

The NIR spectra are linear with density of natural gas components, variations in pressure, temperature and composition introduce only minor difficulties. This fact eliminates the need to calibrate the sensor in a range of pressures, temperatures and compositions. The absorbance spectra of individual pure components, recorded at standard temperature and pressure conditions, can be used to develop a calibration matrix, which can be used to predict the properties of hydrocarbon fuel streams at any pressure, temperature and with any composition.

As the heating value is always measured corresponding to standard temperature and pressure (STP) conditions, it will be convenient to scale to the experimentally measured spectra to the STP conditions. NIST uses a temperature of 293.15 K (20 °C, 68 °F) and an absolute pressure of 101325 Pa (14.696 psi, 1 atm) as standard conditions. Suppose that the pressure, temperature and absorbance are P , T and $A(\lambda)$ respectively. The measured spectra can be scaled to match the spectra at the reference conditions by substituting the values of standard pressure and temperature as $P_0 = 101325$ Pa and $T_0 = 293.15$ K in Eq. 4.10.

$$A_0(\lambda) = A(\lambda) \times \frac{P_0}{P} \times \frac{T}{T_0} \times \frac{Z}{Z_0} = A(\lambda) \times \frac{101325}{P} \times \frac{T}{293.15} \times \frac{Z}{Z_0} \quad (4.11)$$

Here, Z_0 and Z are calculated using the Stewart, Buckhardt, and Voo mixing rules with a correction suggested by Thomas Buxton et al. [23] to calculate pseudocritical properties of hydrocarbon mixtures. This is discussed in detail in the next chapter. During calibration, the scaled spectra are recorded in a database and the spectral data is used to form regression equations to predict the properties of unknown mixtures. The algorithm for predicting the

composition and heating value for variation in the flow stream conditions is depicted in Fig. 4.6.

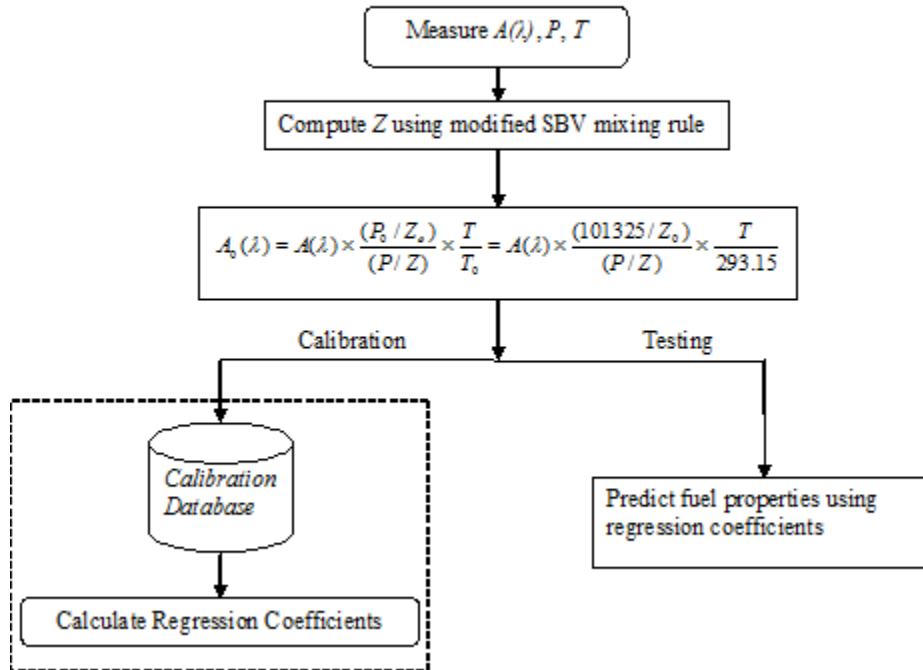


Fig. 4.6 Schematic flow diagram of fuel properties calculation procedure

4.5 Characterization of Landfill Gas Flowing at Elevated Pressures

The prediction accuracy of the density correction algorithm was tested on landfill (methane-carbon dioxide-nitrogen) gas mixtures. The sensor was calibrated at 1 bar using the mixtures shown in Table 6. During prediction testing, the pressure of the flow stream was varied in the desired range using a back pressure regulator. Fig. 4.7 shows the results of the test. The results show that with the density correction algorithm, the prediction accuracy is around 0.5%.

Table 6. Calibration matrix used for validation of density correction algorithm.

Sample #	Methane, %	CO ₂ , %	Set HV
1	38	57	385.2
2	40	56	405.5
3	41	54	415.6
4	43	54	435.9
5	45	50	456.1
6	47	48	476.3
7	49	46	496.5
8	51	44	516.8
9	53	42	537
10	55	40	557.2
11	57	39	577.5
12	59	39	597.8
13	61	39	618.1
14	63	35	638.2
15	65	34	658.5
16	67	33	678.7

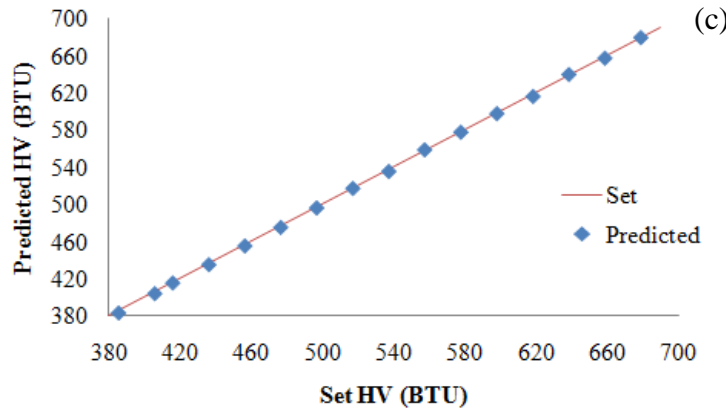
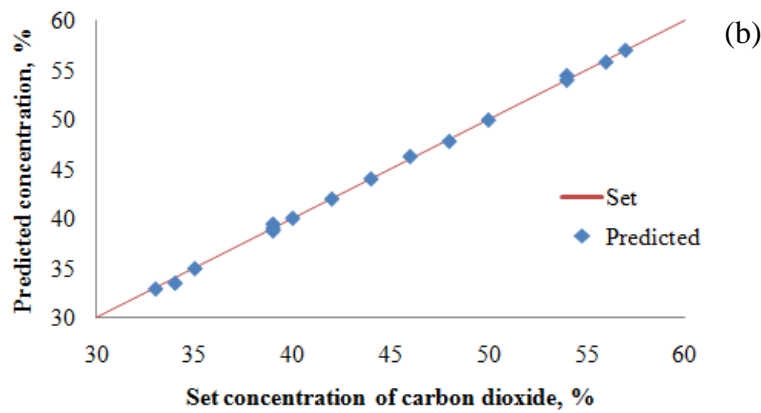
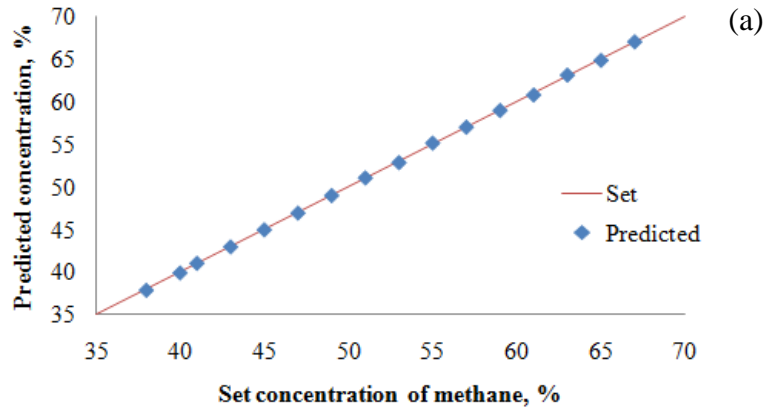


Fig. 4.7 Prediction accuracy of density correction algorithm (a) methane (b) carbon dioxide (c) heating value

5. ACCOUNTING FOR COMPRESSIBILITY OF HYDROCARBON FUELS

5.1 Compressibility of Hydrocarbons Mixtures

The ideal gas equation of state, which can be derived using statistical thermodynamics or experimental measurements, is valid only at low densities. Low density implies no molecular interaction (no forces between molecules) and that the particles occupy no volume (point masses). The ideal gas equation of state does not account for attractive forces and thus cannot predict condensation (i.e. liquid phase). The compressibility factor gives an indication of how much the ideal gas deviates from real gas behavior and is defined as follows:

$$Z = \frac{p\nu}{RT} = \frac{\nu_{act}}{\nu_{ideal}} \quad (5.1)$$

Here, Z is the compressibility factor, ν is the molar volume, R is the gas constant, T is the temperature, ν_{act} is the actual molar volume occupied by the gas and ν_{ideal} is the volume it would have occupied if it was an ideal gas. Compressibility factors are normally obtained from charts, tables of experimental data or empirical correlations. The correlations are either iterative or direct. They differ in accuracy, range of applicability, rate of convergence, computational time and cost. Pitzer et al. introduced the following Eq. (5.2) for pure materials of non-polar nature, which is called a three-parameter principle of corresponding states,

$$Z = f(P_r, T_r, \omega) = Z^{(0)}(P_r, T_r) + \omega Z^{(1)}(P_r, T_r) \quad (5.2)$$

where $Z^{(0)}$ is the compressibility factor of a simple fluid and $Z^{(1)}$ is the deviation of the compressibility factor of the real fluid from $Z^{(0)}$. The data for $Z^{(0)}$ and $Z^{(1)}$ appear in the Lee-Kesler tables and are universal functions of reduced pressure P_r and temperature T_r . The

acentric factor ω is the increase in slope of the vapor pressure versus temperature compared to that of an inert gas. It represents the effect of molecular structure, for example, globular or non-spherical shapes, polar moments and quantum deviations. The reduced properties are defined as follows:

$$P_r = \frac{P}{P_c} \quad (5.3)$$

$$T_r = \frac{T}{T_c} \quad (5.4)$$

The three parameter principle of corresponding states cannot be directly applied to gaseous mixtures. Because of the physical/chemical interaction between the component fluids, the critical properties of mixtures need to be corrected, so that Eq. 5.2 can be used to calculate Z of the mixture as a whole. There are a number of combination rules proposed for determining the pseudocritical constants of gaseous mixtures. The most commonly used is Kay's rule which assumes that pseudocritical pressure and temperature are simply mole fraction averages of the critical properties of pure components,

$$P_c = \sum_i x_i P_{ci} \quad (5.5)$$

$$T_c = \sum_i x_i T_{ci} \quad (5.6)$$

where P_c, T_c are the critical pressure and temperature of the mixture, x_i is the mole fraction and P_{ci}, T_{ci} are the critical pressure and temperature of each individual component. Use of Eq. (5.5) is satisfactory; however the use of Eq. (5.6) results in considerable error. Many other pseudocritical constant rules have been proposed and are widely used in engineering work. Generally, these rules are considerably more complex than Kay's rule and involve

different simplifying assumptions. Comparison of predicted and experimental compressibility factors of natural gas mixtures shows that Stewart, Buckhardt and Voo (SBV) mixing rule gives the most satisfactory values of pseudocritical constants. According to this rule, pseudocritical properties are given by the following equations.

$$J = \frac{T_{pc}}{P_{pc}} = \frac{1}{3} \sum_i y_i \left(\frac{T_c}{P_c} \right)_i + \frac{2}{3} \left[\sum_i y_i \left(\frac{T_c}{P_c} \right)_i^2 \right]^{1/2} \quad (5.7)$$

$$K = \frac{T_{pc}}{P_{pc}^{1/2}} = \sum_i y_i \left(\frac{T_c}{P_c^{1/2}} \right) \quad (5.8)$$

$$T_{pc} = \frac{K^2}{J} \quad (5.9)$$

$$P_{pc} = \frac{P_{pc}}{J} \quad (5.10)$$

Where y_i are mole fractions; T_c , P_c are critical properties of individual components.

5.2 Compressibility of Hydrocarbons–Carbon Dioxide Mixtures

For lean natural gas mixtures (natural gas mixtures with low concentrations of heavy hydrocarbons and containing carbon dioxide), the compressibility factors predicted using SBV mixing rule have large deviation from experimental data. There are several methods proposed, which introduce additional parameters to the principle of corresponding states to calculate the compressibility factor of lean natural gas mixtures. A method proposed by Thomas Buxton et al. [23] is selected for the heating value sensor. Between dissimilar hydrocarbon molecules dispersion forces predominate, however between two carbon dioxide molecules, a quadruple force predominates. This method introduces a new parameter called,

multipole factor, to correct pseudocritical constants of binary hydrocarbon–carbon dioxide mixtures. The results have been compared with experimental data for CH₄–CO₂, C₂H₆–CO₂, C₃H₈–CO₂ and C₄H₁₀–CO₂ mixtures. The method works well at high pressures as well. Pseudocritical pressure P_{pc} and temperature T_{pc} are determined graphically from a plot of experimental Z versus reduced pressure P_r . Fig. 5.1 shows the difference between graphically determined T_{pc} and T_{pc} determined using SBV mixing rule as a function of carbon dioxide concentration. This difference is called multipole factor τ . For multicomponent mixtures containing more than one hydrocarbons and carbon dioxide, the mixture can be treated as a binary mixture of all hydrocarbons together and carbon dioxide. The accentric factor of hydrocarbon mixture ω_h is determined using Eq. (5.11). Fig. 5.2 and Fig. 5.3 show the plot of multipole factor as a function of hydrocarbon accentric factor for different concentrations of carbon dioxide.

$$\omega_h = \frac{\sum_j y_j \omega_j}{\sum_j y_j} \quad (5.11)$$

The graphically determined multipole factor and hydrocarbon accentric factor are used to adjust pseudocritical properties computed using SBV rule.

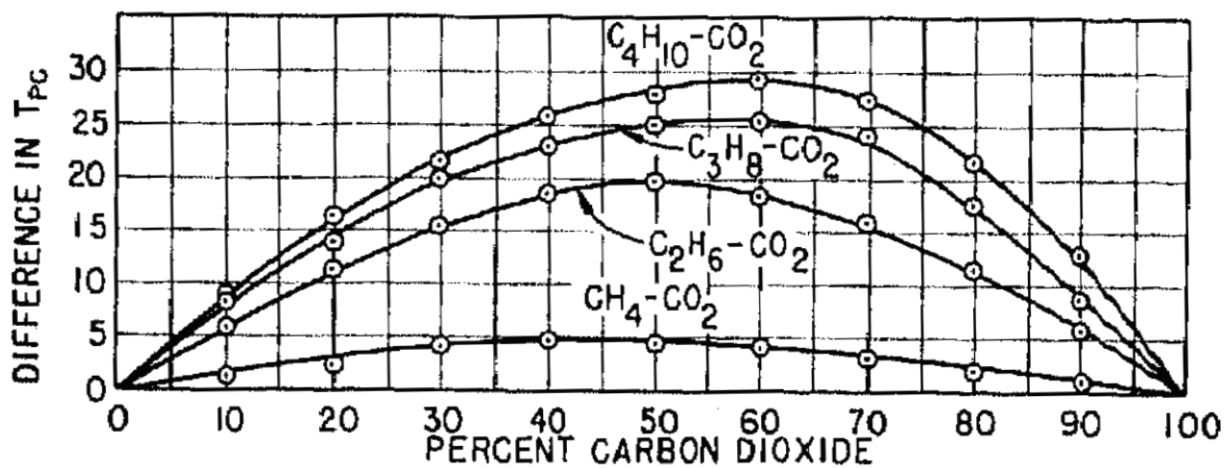


Fig. 5.1 SBV T_{pc} minus graphically determined T_{pc} as a function of concentration of carbon dioxide [23]

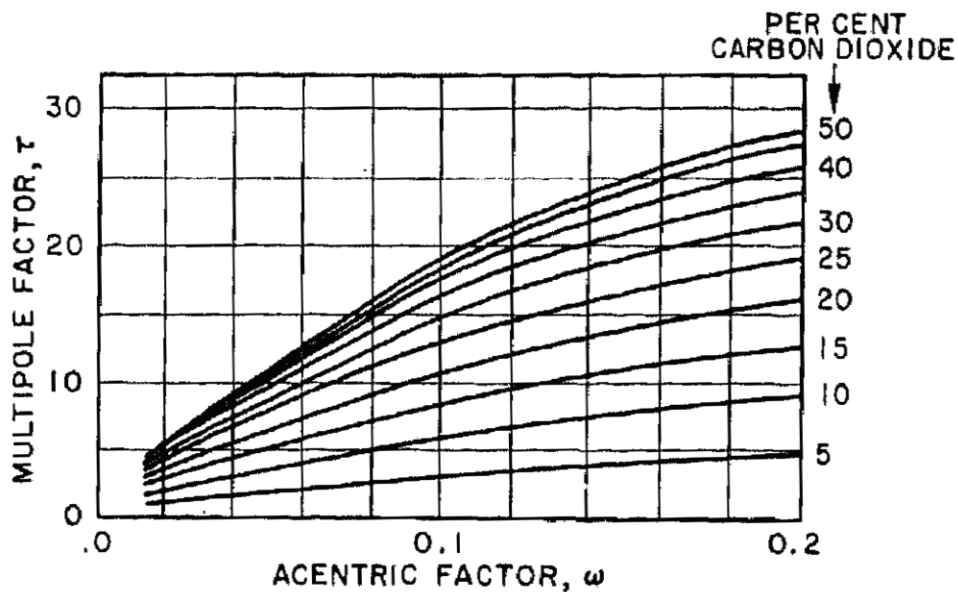


Fig. 5.2 Multipole factor versus hydrocarbon acentric factor for 5 to 50% CO₂ [23]

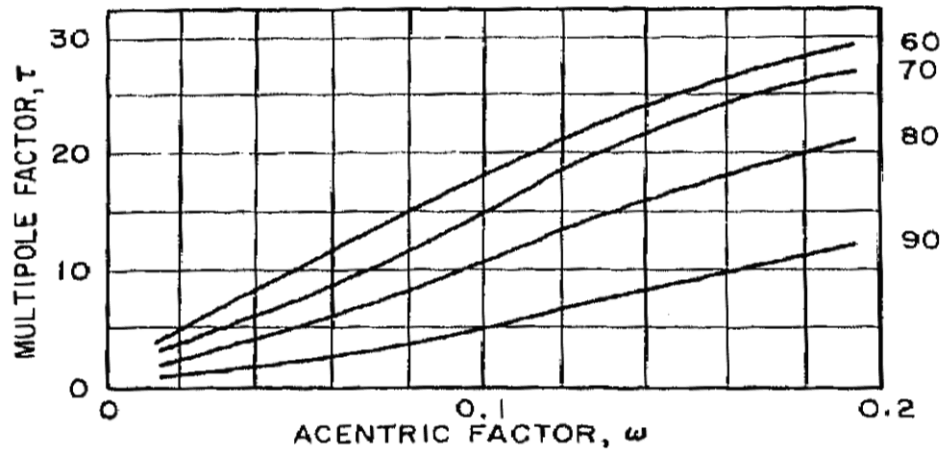


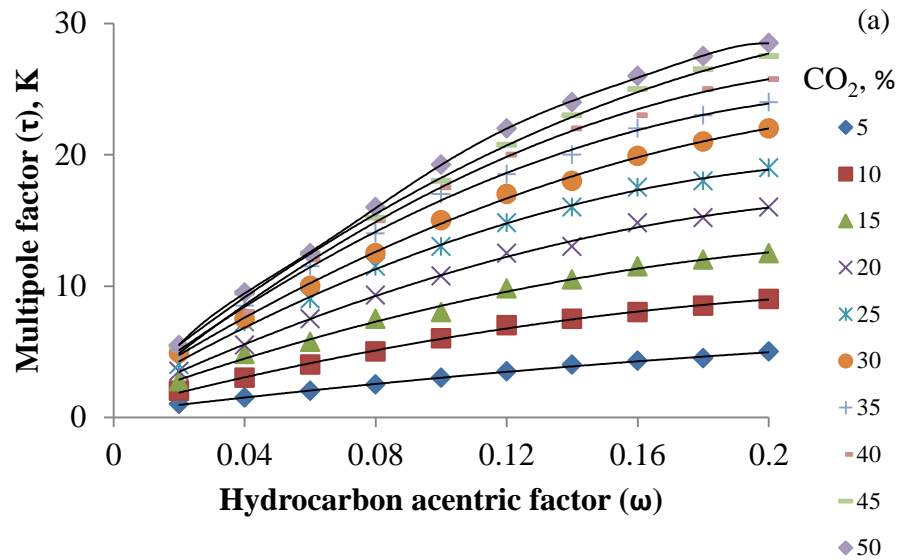
Fig. 5.3 Multipole factor versus hydrocarbon acentric factor for 60 to 90 % CO₂ [23]

Below is the step-by-step procedure to calculate the compressibility factor of a lean natural gas-carbon dioxide and landfill gas mixture.

1. Calculate the pseudocritical pressure and critical temperature using Eq. (5.7) to (5.10).
2. Determine the hydrocarbon mixture acentric factor using Eq. (5.11).
3. Read τ from Fig. 5.2 or Fig. 5.3 for the desired concentration of carbon dioxide and hydrocarbon acentric factor. To reduce computational time, polynomials of appropriate order (3rd or higher, up to 6th) are fitted to the data in Fig. 5.2 and Fig. 5.3 by minimizing the residual error and using the best fitted coefficients, the multipole factor τ is determined (numerically rather than graphically). Table 7 shows the values of τ as a function of ω and carbon dioxide concentration. Fig. 5.4 shows the polynomial curves fitted to the data given in Table 7.

Table 7. Multipole factor as a function of acentric factor and carbon dioxide concentration.

ω	Carbon Dioxide Concentration (%)									
	5	10	15	20	25	30	35	40	45	50
0.02	1	2	2.75	3.5	4	4.9	5	5.2	5.4	5.5
0.04	1.5	3	4.8	5.5	7.25	7.5	8.5	8	9.5	9.5
0.06	2	4	5.75	7.5	9	10	11.5	12	12.5	12.5
0.08	2.5	5	7.5	9.3	11.5	12.5	14	15	15.2	16
0.1	3	6	8	10.75	13	15	17	17.5	18	19.25
0.12	3.5	7	9.8	12.5	14.8	17	18.5	20	20.75	22
0.14	4	7.5	10.5	13	16	18	20	22	23	24
0.16	4.3	8	11.5	14.8	17.5	19.9	22	23	25	26
0.18	4.5	8.5	12	15.2	18	21	23	25	26.5	27.5
0.2	5	9	12.5	16	19	22	24	25.75	27.5	28.5



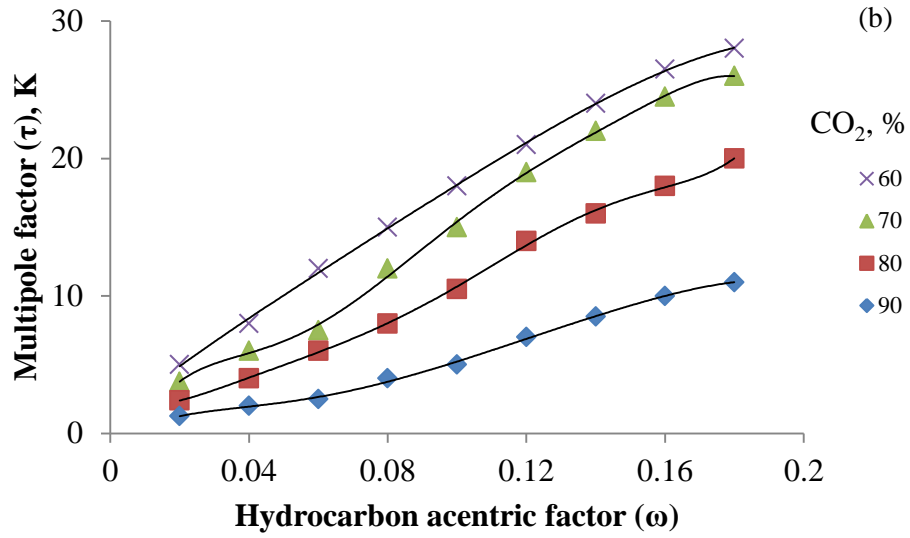


Fig. 5.4 Polynomial curves fitting for numerical determination of multipole factor

4. Calculate the adjusted pseudocritical constants from Eq. (5.12),

$$T_{pc}' = T_{pc} - \tau$$

$$P_{pc}' = P_{pc} \times \frac{T_{pc}'}{T_{pc}} \quad (5.12)$$

5. Find the total mixture acentric factor using Eq. (5.13), where the summation is now taken over all the components,

$$\omega' = \sum_i y_i \omega_i \quad (5.13)$$

6. For the temperature and pressure of the system, calculate pseudoreduced properties,

$$T_{pr} = \frac{T}{T_{pc}'} \quad (5.14)$$

$$P_{pr} = \frac{P}{P_{pc}} \quad (5.15)$$

7. With these pseudoreduced properties, $Z^{(0)}$ and $Z^{(1)}$ may be read from Lee-Kesler tables or graphs. Alternately, these values can be computed using the following empirical relations,

$$Z^{(0)} = 1 + \left(0.083 - \frac{0.422}{T_{pr}^{1.6}} \right) \frac{P_{pr}}{T_{pr}} \quad (5.16)$$

$$Z^{(1)} = \left(0.139 - \frac{0.172}{T_{pr}^{4.2}} \right) \frac{P_{pr}}{T_{pr}} \quad (5.17)$$

$$Z = Z^{(0)} + \omega' Z^{(1)} \quad (5.18)$$

5.3 Predicting the Concentrations of NIR Inactive Components in a Fuel Mixture

Since the NIR inactive gases present in the fuel mixture, such as, nitrogen, cannot be detected in this spectral region, the predicted concentrations of hydrocarbons and carbon dioxide can be used as an initial approximation to compute the molar concentration per unit volume considering the compressibility factor. These calculated concentrations can then be used to calculate the percentage concentration of each individual component. If the predicted and computed percentage concentrations are not close enough, the computed percentage concentrations can be used in the next iteration to re-calculate the compressibility factor. A number of iterations can be performed to achieve a desired accuracy level in the predicted concentrations. This step-by-step procedure is listed below and Fig. 5.5 shows the schematic flow diagram of this procedure.

1. Use the predicted concentrations of hydrocarbons to calculate the compressibility factor of the mixture.
2. Suppose, Z_i is the compressibility factor of i^{th} component at a pressure N_i*P , then, the actual partial pressure of each component can be computed using the following equation,

$$P_i = \frac{N_{i,predicted}Z_iP}{Z} \quad (5.19)$$

3. Calculate the percentage error ε in measured and calculated total pressure of the mixture,

$$\varepsilon = \frac{P - \sum P_i}{P} \times 100 \quad (5.20)$$

4. If $|\varepsilon| \leq 0.5\%$, we can conclude that the predicted concentrations are within acceptable accuracy. If $\varepsilon > 0.5\%$, it implies that the real composition is more compressible than the predicted composition. In this case, we need to increment the predicted concentrations of hydrocarbons, which are present in the mixture (components for which predicted concentration $N_{i,fuel} > 0$) by a small step, say 1%. Then we recompute the mole fractions and the compressibility factor. If $\varepsilon < -0.5\%$, reduce the predicted concentrations of hydrocarbons by 1%, recompute the mole fractions and the compressibility factor. Repeat steps 2, 3 and 4 until the desired accuracy is achieved in predicted concentrations.

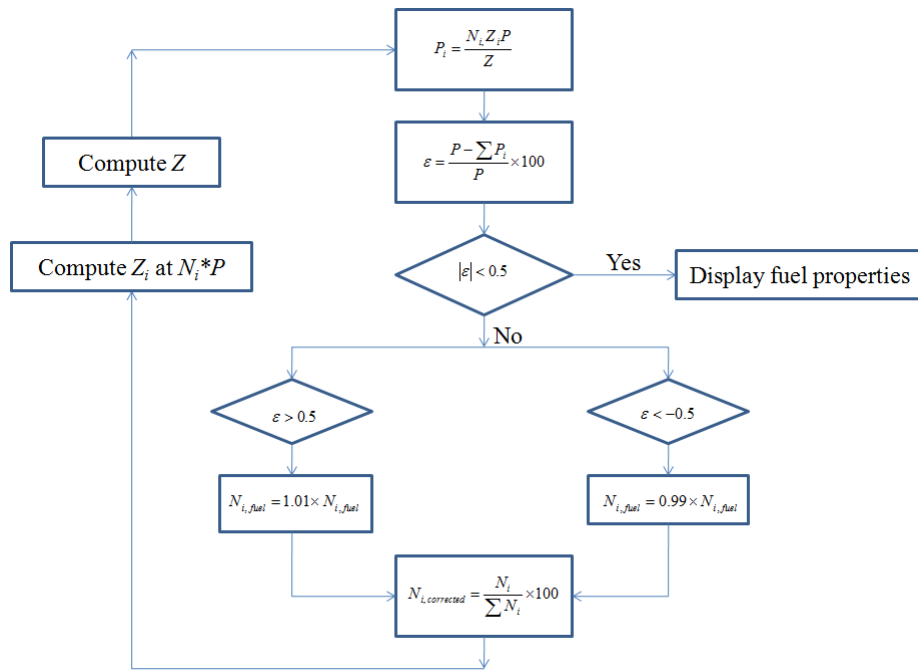


Fig. 5.5 Schematic flow diagram of procedure for correcting the compressibility factor programmatically

5.4 Experimental Determination of the Compressibility Factor of Hydrocarbon Mixture

It is necessary to experimentally verify the accuracy of the above algorithm at correcting the predicted composition of hydrocarbon mixtures. In this experiment, to determine the compressibility factor accurately, the mixture must be prepared with high accuracy. The composition and pressure of the mixture are constrained by the specifications of the flow control system used in the experiment. MKS Mass Flow Controllers (MFCs) had an accuracy of 1% of full scale and the maximum pressure allowed at the inlet of the MFCs was 11.36 bar (150 psig). The MFCs had full scale ratings of 1000, 2000 and 5000 SCCM, resulting in an

error in mixture preparation of 1.7%. The gas correction factor for propane is the lowest (0.36) and thus, it was connected to the MFC having maximum full scale rating (5000 SCCM). Methane has a gas correction factor of 0.72 and was connected to the MFC having full scale rating 2000 SCCM. Thus, the resulting mixture composition was 33.96% methane, 42.45% propane and 23.58% nitrogen. The sensor was initially calibrated with pure methane and pure propane. Taking the weighted sum of pure spectra, the spectrum of a mixture of 50% methane and 50% nitrogen was calculated and this spectrum was also added to the calibration database. The regression coefficients were computed using 2 principal components (2 absorbing components – methane and propane). Fig. 5.6 shows the NIR spectrum of the mixture measured at 8.78 bar (127.33 psi) and 300 K (27 °C).

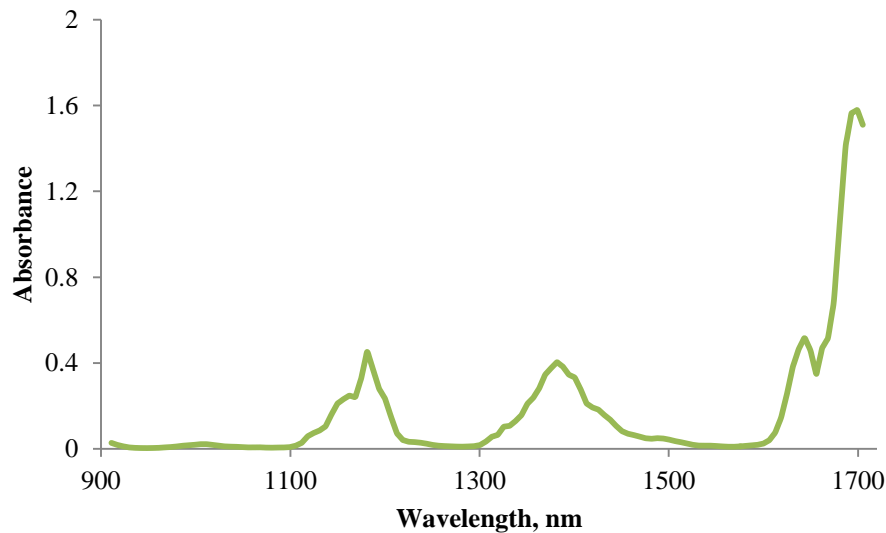


Fig. 5.6 NIR absorption spectrum of a mixture of 33.96% methane, 42.45% propane and 23.58% nitrogen at 8.78 bar and 300 K

All the spectra are corrected to standard conditions before multivariate analysis. Using the corrected spectra, the PCR predicted composition was 33.69% methane, 42.83% propane and 23.48% nitrogen. For this mixture, the multipole factor will be zero, as carbon dioxide is not present in the mixture. Using the modified SBV mixing rule, the compressibility factor is 0.9574. The compressibility factor of the mixture can also be computed using SBV mixing rule (without applying the correction suggested by Thomas Buxton et. al. [23]) and will be equal to that computed using modified SBV mixing rule. The compressibility factor was also computed using AGA-8 (American Gas Association) procedure and was 0.9551. Thus, we can conclude that the modified SBV mixing rule produces adequately accurate values of the compressibility factor (-0.24% error in the case of the mixture used in this experiment). Equation 5.19 was used to compute the partial pressures of individual components. The percentage error in calculated total pressure of the mixture was $\varepsilon = -0.0393\%$ (calculated using Equation 5.20). As $|\varepsilon| < 0.5\%$, it can be concluded that the predicted concentrations are within acceptable accuracy.

6. MINIMIZING TEMPORAL DRIFT OF SPECTRAL DETECTOR

6.1 Determining the Repeatability of Spectral Measurements

6.1.1 Experimental Approach

From standpoint of industrial application of the sensor and to minimize the cost of its commercial prototype, a low-cost, low resolution detector was used. To study the precision of the sensor, it becomes necessary to determine the repeatability/reproducibility of spectral measurements to allow calculations of the predicted fuel properties. The potential sources of systematic uncertainties in spectral measurements can be identified as:

- 1) Variation in the temperature of the light source with time
- 2) Variation in the reference intensity, due to variation in the temperature of light source
- 3) Variation in the background noise level
- 4) Drift in the detector sensitivity

These factors will collectively affect the spectral measurements and their reproducibility. An optical setup shown in Fig. 6.1 was used to determine the repeatability of spectral measurements.

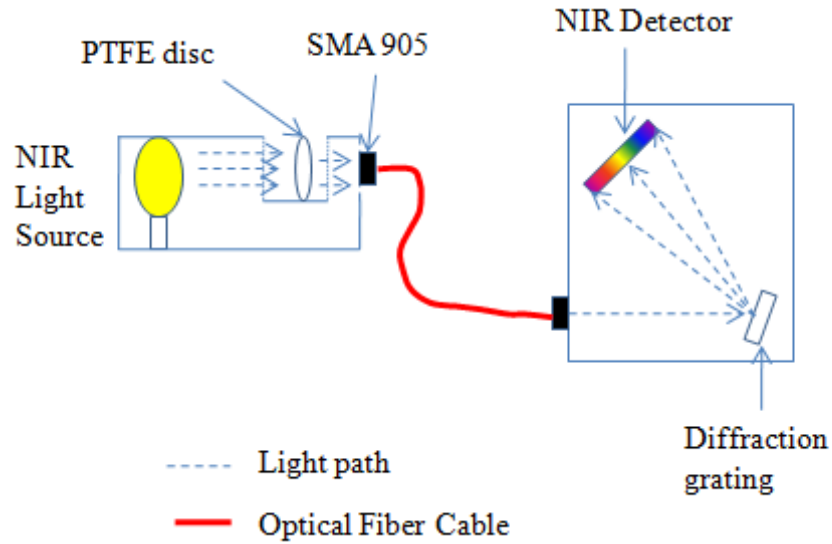


Fig. 6.1 Optical setup to determine repeatability of spectral measurements

6.1.2 Experimental Procedure

- 1) Switch on and warm up the spectroscopic sensor and light source.
- 2) Acquire and store the background noise level.
- 3) Acquire and store the reference intensity (intensity without a sample between source and detector).
- 4) Acquire and store the transmitted intensity/absorption spectrum of a sample (PTFE diffusing disc was used in this case).
- 5) Repeat the same procedure for desired number of tests.

For each measurement, 100 scans of intensity were averaged. The above test procedure was performed 11 times (1 each day). The spectra are shown in Fig. 6.2. If we consider any two

spectra, a constant shift in the absorbance in the entire spectral region can be visually observed.

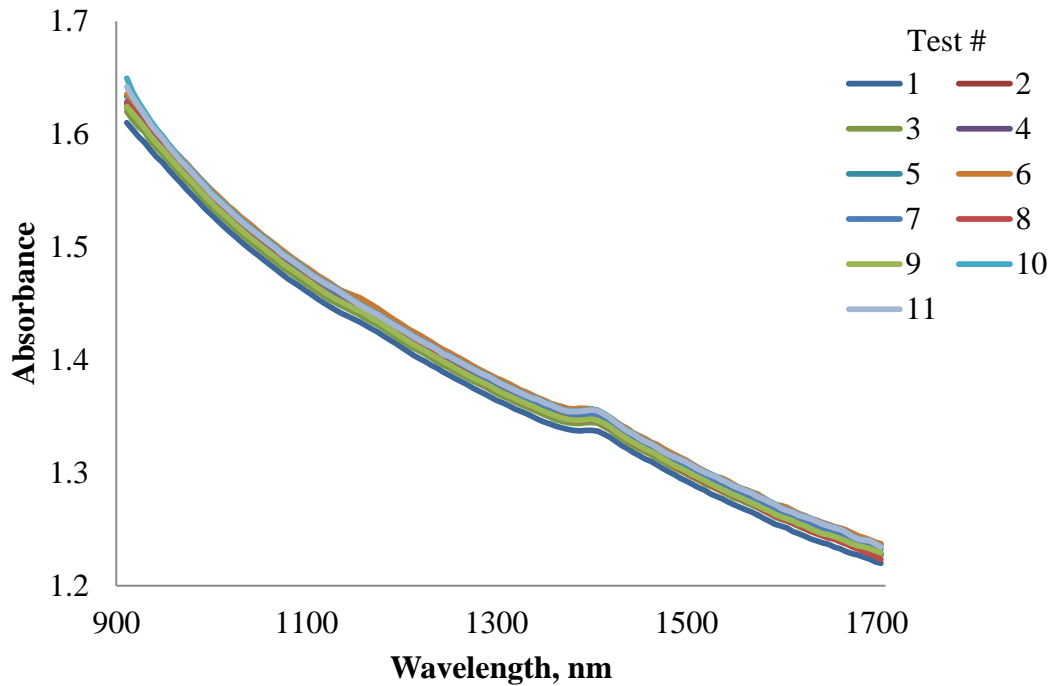


Fig. 6.2 Example of a typical temporal drift distribution of a sensor during 11 days of measurement

6.1.3 Results and Conclusion

In order to compute the repeatability/reproducibility of the measured spectra, four random wavelengths, 1000, 1400, 1481 and 1600 nm, were selected from the considered range. The percentage relative error in absorbance measured at each of these wavelengths was plotted against Test #. From Fig. 6.3, it can be concluded that the repeatability of absorbance measurement is $\pm 0.5\%$.

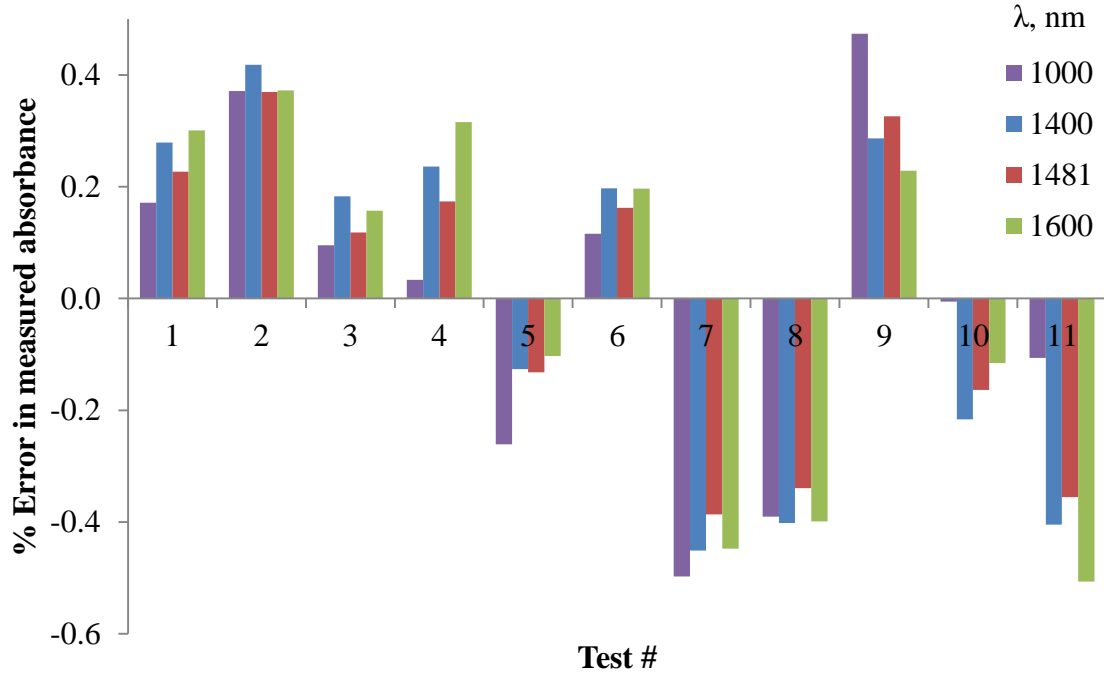


Fig. 6.3 Percentage error in measured absorbance

6.2 Effect of Optical Instabilities on Prediction Error

In order to assess the effect of spectral instabilities on prediction of fuel mixtures, four tests were conducted using landfill gas mixtures on consecutive days using the calibration matrix developed on the first day. Table 8 shows the average absolute percentage errors in the predicted properties. It can be clearly seen that the prediction error was the least in the first test and increased in subsequent tests (Fig. 6.4). The prediction error is defined using Eq. 6.1.

$$Prediction\ error = \frac{\sum \left| \frac{n_{i,set} - n_{i,predicted}}{n_{i,set}} \times 100 \right|}{m} \quad (6.1)$$

Table 8. Average absolute percent prediction error.

	Methane	CO₂	HV
Test 1	0.16119	0.39275	0.15697
Test 2	0.22147	0.3794	0.24124
Test 3	0.38035	2.3461	0.32308
Test 4	0.52561	3.49246	0.438

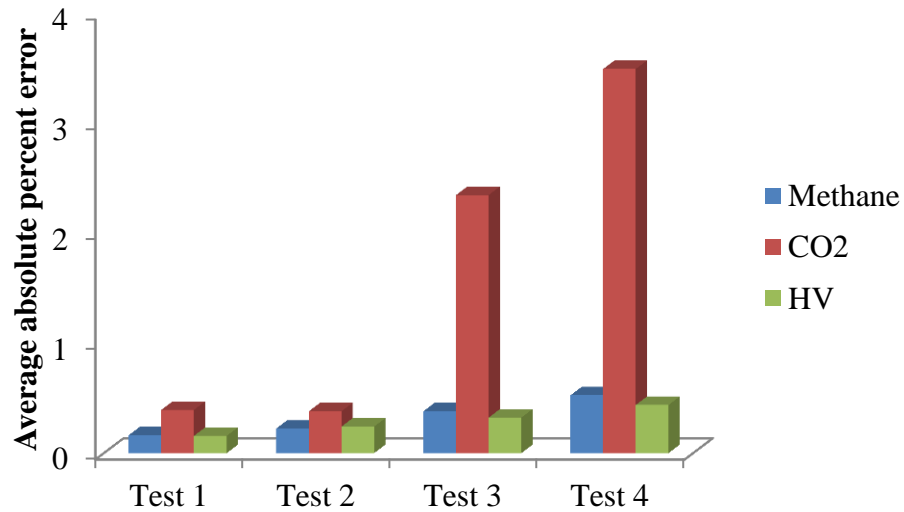


Fig. 6.4 Prediction error

6.3 Temporal Drift in Spectra due to Optical and Electronic Instabilities

The previous tests suggest a temporal drift in spectral measurements. This drift results in a poor reproducibility of sensor signal, making frequent calibration of the system necessary. The objective of this experiment is to establish a simple mathematical algorithm that allows a quick calibration of the measurement data to compensate for both short-term (hours) and long-term (days, months) sensor drift. The data obtained from two different experiments was

used for investigation of the sensor drift. The spectra of two pure species – carbon dioxide and methane at ambient conditions – were recorded and the temporal response of the NIR detector was studied. Fig. 6.5 (a) shows the temporal drift in the absorbance spectrum of carbon dioxide. Fig. 6.5 (b) shows the temporal drift in absorbance at sample wavelengths. The same drift is found with methane, however, due to the higher order of magnitude of absorbance, this drift cannot be visually observed in methane spectra. Fig. 6.6 shows the lineplot of drifting response signals during 4 days of measurement (five measurements each day). A day-to-day variation of the sensor response can be seen from these measurements.

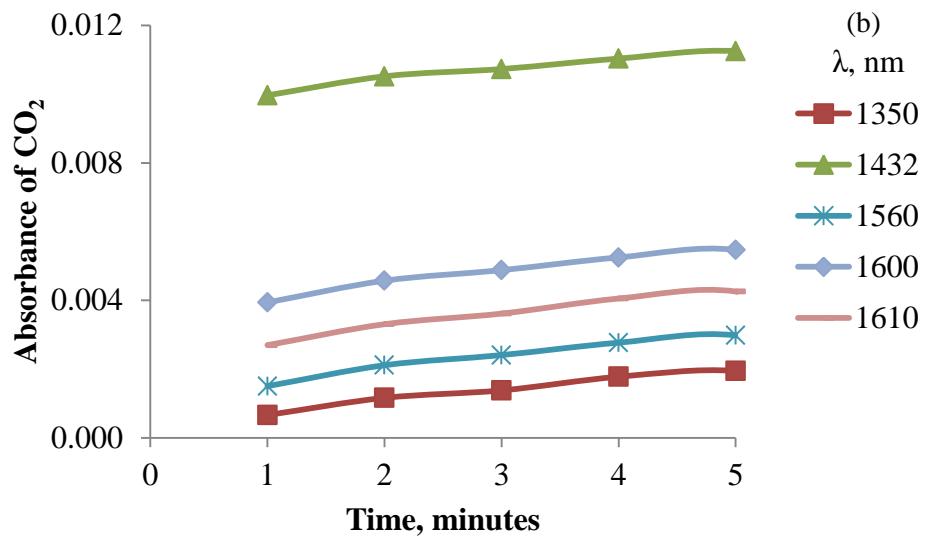
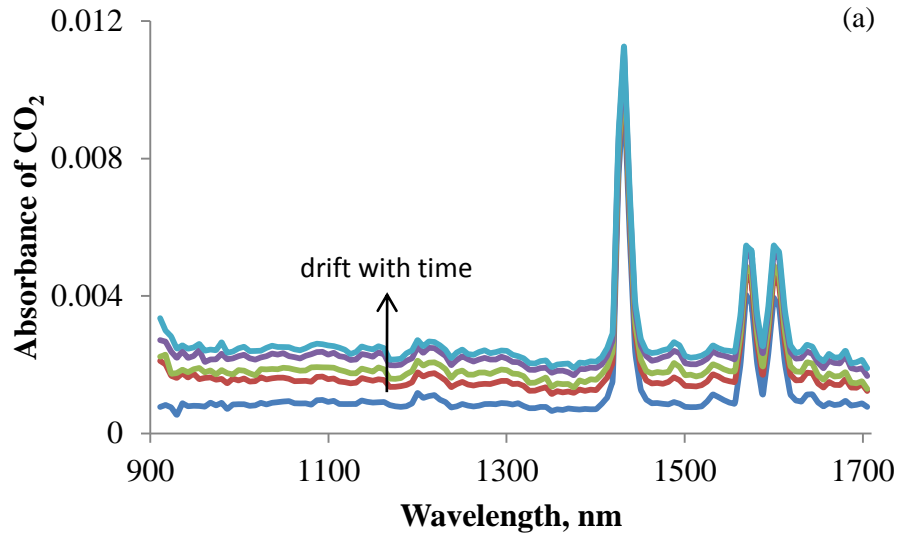


Fig. 6.5 Example of a typical temporal drift of a NIR detector based on repeated measurements

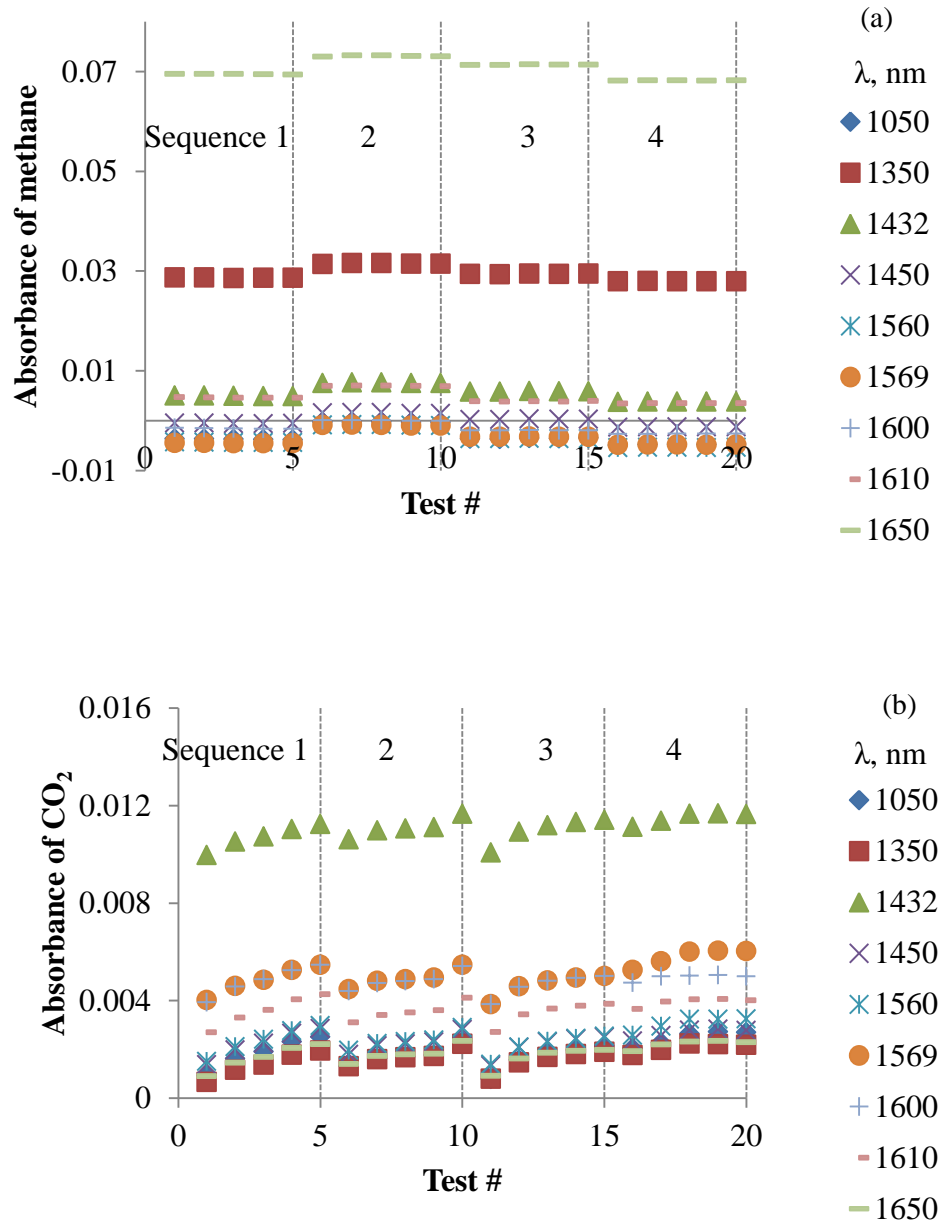


Fig. 6.6 Lineplot with drifting response signals during four days of measurement (Sequence 1

- 4)

6.4 Drift Correction

The basic idea of drift compensation algorithm is to eliminate the variation in the signal ascribed to sensor drift. Consider the absorption spectra of carbon dioxide shown in Fig. 6.5 (a). The drift in the spectra is a resultant effect of variation in light source temperature and hence reference intensity, variation in the background noise level and detector sensitivity drift. Consider the intensity measurements in a wavelength range λ_1 to λ_3 (Fig. 6.7). Suppose that absorption of light occurs only in the region λ_1 to λ_2 ($\lambda_1 < \lambda_2 < \lambda_3$). The reference intensity is recorded at time t_1 and absorbance spectrum is recorded at time t_2 .

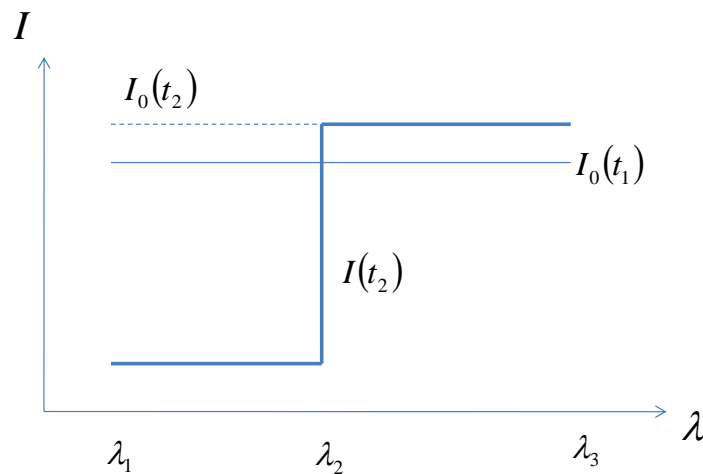


Fig. 6.7 Temporal drift in the reference intensity

The absorbance A' at an absorbing wavelength λ_l is given by,

$$A' = \log \left[\frac{I_0(t_1)}{I(t_2)} \right] \quad (6.2)$$

Ideally, $I_0(t_1) = I_0(t_2)$; however, due to the combined effect of light source temperature and detector sensitivity, the reference intensity can be assumed to be shifted to a different value. The detector sensitivity drift is a function of time and wavelength as well. This change in the reference intensity results in non-zero absorbance A^* at a non-absorbing wavelength λ_3 and is given by,

$$A^* = \log \left[\frac{I_0(t_1)}{I_0(t_2)} \right] \quad (6.3)$$

The true absorbance A at wavelength λ_1 at time t_2 can be calculated as,

$$A = A' - A^* = \log \left[\frac{I_0(t_1)}{I(t_2)} \right] - \log \left[\frac{I_0(t_1)}{I_0(t_2)} \right] = \log \left[\frac{I_0(t_2)}{I(t_2)} \right] \quad (6.4)$$

The error $A^*(\lambda)$ can be computed by fitting a polynomial to the spectra measured in all non-absorbing wavelength ranges. For example, for carbon dioxide, $A^*(\lambda)$ can be computed by fitting a polynomial to the absorbances measured in the wavelength region 900 nm to 1150 nm, 1300 to 1350 nm and for methane, these wavelength ranges can be 1200 nm to 1300 nm and 1500 nm to 1600 nm. The polynomials are fitted by minimizing the residual error and the best fit coefficients are used to compute the error $A^*(\lambda)$. Fig. 6.8 (a) shows a typical measured absorption spectrum of carbon dioxide at ambient conditions. Fig. 6.8 (b) shows a polynomial fitted to $A^*(\lambda)$ measured at non-absorbing wavelengths. This polynomial represents the drift in the spectrum above/below the true value. From Fig. 6.8 (c), it can be easily seen that the drift-corrected absorbance equals zero in non-absorbing wavelength ranges. Fig. 6.9 (a) shows five drift corrected absorption spectra recorded during five consecutive measurements, which very well overlap each other, thereby, proving the

repeatability of the measurements. Fig. 6.9 (b) shows the corrected absorbances at selected wavelengths. It can be clearly seen that the absorbance at each wavelength remains constant.

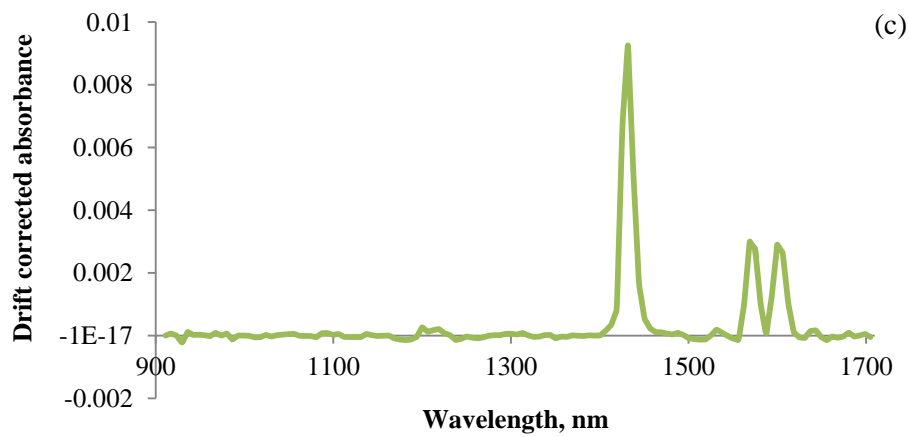
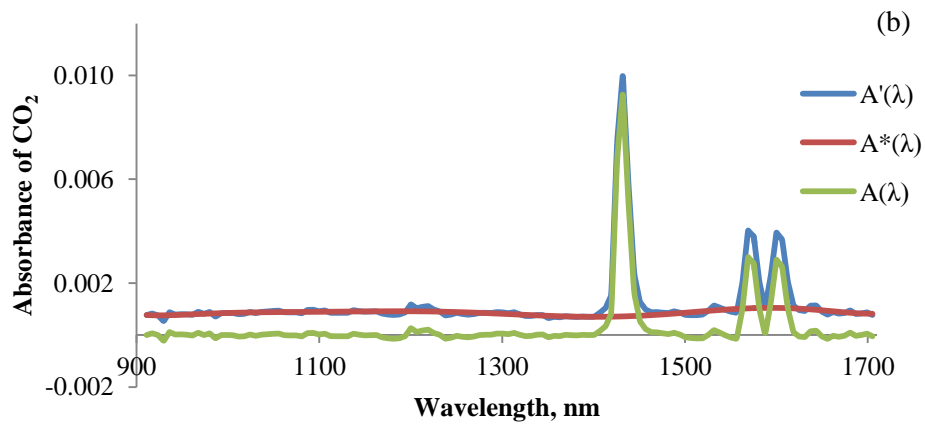
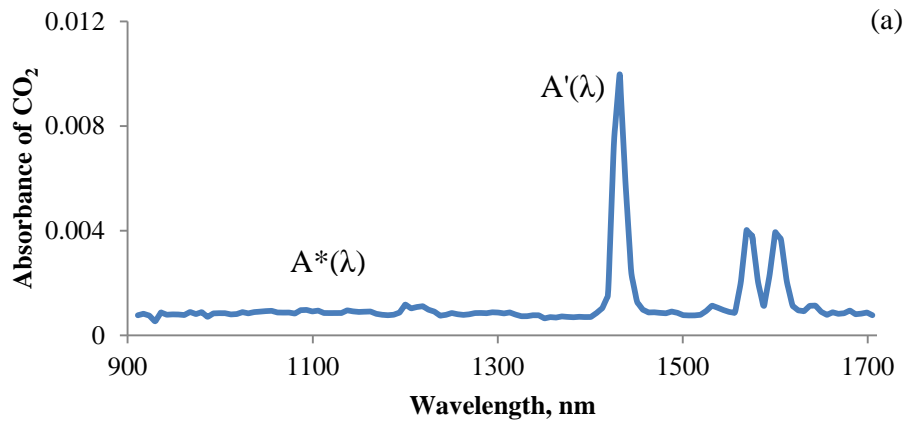


Fig. 6.8 Drift correction of measured spectra

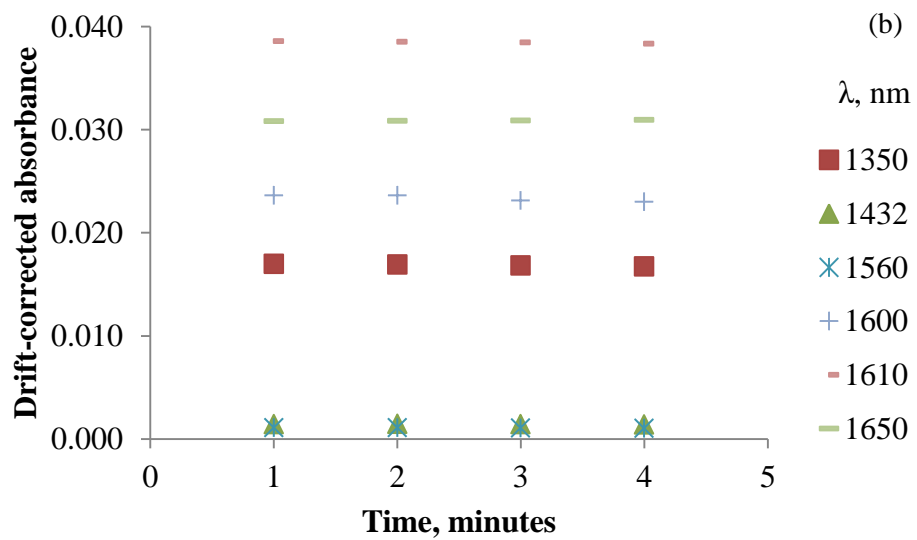
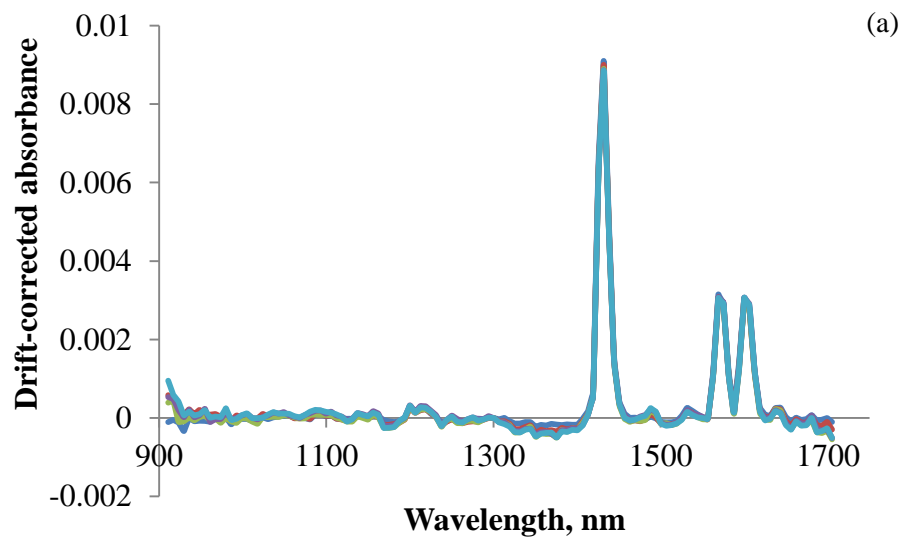


Fig. 6.9 Drift correction in multisequence measurements

Alternately, the reference intensity $I_0(t_2)$ can be computed using the fact that the intensity at non-absorbing wavelengths should be equal at times t_1 and t_2 . Fig. 6.10 shows a typical reference intensity curve. A polynomial curve can be fitted to the sample intensities $I(t_2)$ at non-absorbing wavelengths by minimizing the residual error (Fig. 6.11) and the best fit coefficients can be used to predict the true reference intensity $I_0(t_2)$ at absorbing wavelengths. The computed reference intensity $I_0(t_2)$ and the measured sample intensity $I(t_2)$ can be used to calculate the true spectrum using Eq. 6.4. The disadvantage of this method is that it is comparatively more complex and requires more computational time. Due to the nature of the reference intensity curve, a large number of data points and a very high order of the polynomial need to be selected. Alternately, the entire considered spectral region can be divided into short wavelength ranges and a comparatively lower order polynomial can be fitted in each of these ranges.

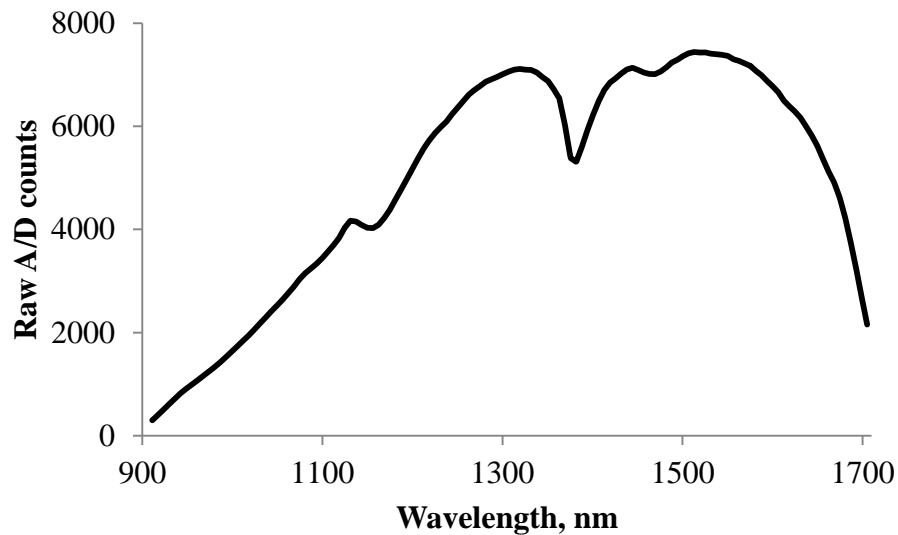


Fig. 6.10 Reference intensity I_0

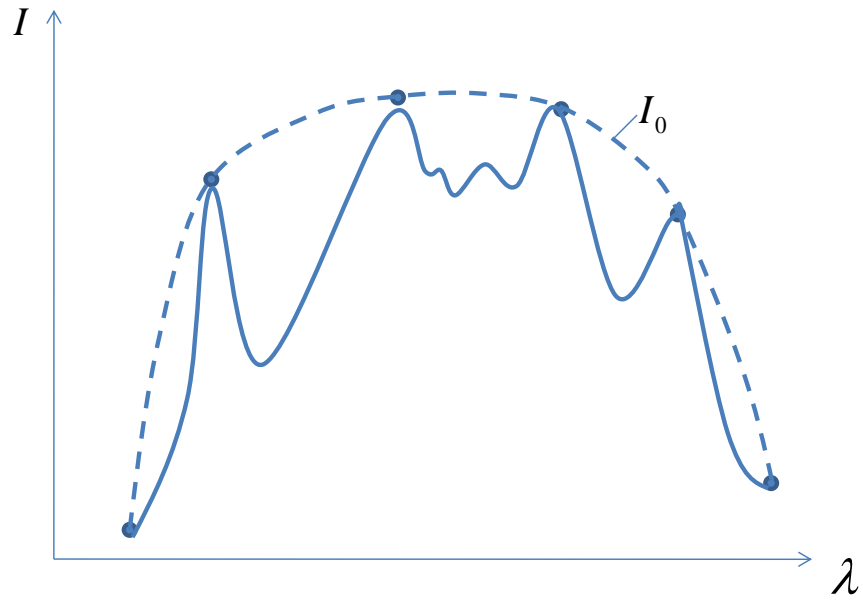


Fig. 6.11 Reference intensity reconstruction

CONCLUSIONS

NIR spectroscopy has been widely used as the method of choice in field applications. For spectroscopic characterization of hydrocarbons-carbon dioxide mixtures, the question arises whether there is any spectral nonlinearity in the wide range of pressure, temperature and composition variation in the field applications. I have established here that with a low resolution spectroscopic detector having instrumental line width greater than the natural line widths in the considered spectral region, undesired sensitivity to pressure and temperature changes can be eliminated and linearity in the NIR spectra with density can be obtained. A simple formulation of Beer's law can be employed to extract the composition information from the NIR spectrum of a mixture. The spectral effects such as line broadening and shift do not have significant impact on the spectra in the pressure and temperature range considered. The linearity in the spectra also minimizes the calibration requirements. One-time calibration with NIR spectra of pure components, viz., methane, ethane, propane, butane and carbon dioxide is adequate for characterizing the mixtures. At elevated pressures and temperatures, the compressibility factor becomes significant and must be considered to correct the NIR spectra. The compressibility factors of hydrocarbon-carbon dioxide mixtures can be determined using SBV mixing rule with a correction suggested by T. Buxton et. al. The compressibility factors calculated using modified SBV mixing rule are very close to those calculated using AGA-8 method. Also, short-term and long-term temporal drift in the spectra due to optical instabilities such as, variation of light source temperature, light intensity, background noise level, and detector sensitivity drift, can be mathematically corrected using

a simple algorithm. The NIR data acquisition, processing, correction for density, compressibility and temporal drift is done in real time using a software developed in LabVIEW. The predicted composition and heating values have 1% accuracy for natural gas and landfill gas mixtures. This also shows the predictive power of multivariate calibration methods – partial components regression (PCR) and partial least squares (PLS). Even with nearly identical NIR spectra of ethane, propane and butane, high accuracy in predicting the fuel properties is achieved. Thus, NIR spectroscopy is definitely a promising, low-cost alternative to gas chromatography.

FUTURE WORK

The NIR technique can be extended to other applications which involve the use of hydrocarbon fuel mixtures, such as, to determine the air-fuel ratio of the mixtures being supplied to internal combustion engines, analysis of monocyclic aromatics of gasoline and gas-oil ratio for crude oils [58]. This technique can also be used in oil wells for *in situ* measurement of the quantity of methane dissolved in crude oil. The hardware used in the NIR setup, i.e., tungsten-halogen lamps, fiber optics, silicon and InGaAs detectors, is operable at elevated pressures and temperatures. Hence, the NIR technique can be utilized in oil wells and similar high pressure/temperature applications. NIR can also be utilized for assessment of essential oil components and the possible detection of adulteration for quality control purposes [59].

REFERENCES

1. http://www.cosa-instrument.com/Products/PDF_Files/Cosa9600Brch.pdf
2. http://www.thermo.com/eThermo/CMA/PDFs/Product/productPDF_50466.pdf
3. <http://precisiongasinstruments.com/>
4. [http://www05.abb.com/global/scot/scot267.nsf/veritydisplay/427f48915cbb63d1852575c50048aed0/\\$File/Analyzer%20Products%20\(dark%20cover\).pdf](http://www05.abb.com/global/scot/scot267.nsf/veritydisplay/427f48915cbb63d1852575c50048aed0/$File/Analyzer%20Products%20(dark%20cover).pdf)
5. http://www.hs-ait.com/Downloads/AIT_family_Brochure.pdf
6. <http://www.postnova.com/PDFDocuments/productinfos/agilent-ch1.pdf>
7. http://www.cosa-instrument.com/Products/PDF_Files/HGC303.pdf
8. <http://www2.emersonprocess.com/siteadmincenter/PM%20Daniel%20Documents/Daniel-Family-of-GC-Brochure.pdf>
9. http://www.germanlloyd.org/pdf/GasPT_DS.pdf
10. http://www.sea.siemens.com/us/Products/Process-Analytics/TechnicalLibrary/Documents/SITRANS_CV_EN.pdf
11. <http://www.precisionpipeline.com/PDF%20Documents/Spectra/SS3000%20Data%20Sheet.pdf>
12. http://www2.emersonprocess.com/siteadmincenter/PM%20Rosemount%20Analytical%20Documents/Gas_PDS_X-STREAM_XEGC_103-XEGC_201001.pdf
13. [http://www.landtecnica.com/uploads/products/68/downloads/GEM2xxxManual\(En\)-RevB1.pdf](http://www.landtecnica.com/uploads/products/68/downloads/GEM2xxxManual(En)-RevB1.pdf)

14. N. Goldstein, M. Gersh, F. Bien, S. Richtsmeier, J. Gruninger, S. Adler-Golden, D. Griffies, C. Ronnenkamp, D. Householder, J. Krogue, and D. Gould, “*Real-time optical BTU measurement of natural gas at line pressure*”, 4th International Symposium on Fluid Flow Measurement, Denver, Colorado, USA, June 27–30, 1999.
15. C. W. Brown and S. C. Lo, "Feasibility of On-line Monitoring of the BTU Content of Natural Gas with a Near-Infrared Fiber Optic System," Appl. Spectroscopy, 47, 812, 1993.
16. http://en.wikipedia.org/wiki/Electromagnetic_spectrum
17. G. R. Fowles, “*Introduction to Modern Optics*”, Dover Publications, Second Edition, 253 – 258, 1975.
18. http://en.wikipedia.org/wiki/Rotational_spectroscopy
19. <http://www.cem.msu.edu/~reusch/VirtualText/Spectrpy/InfraRed/infrared.htm>
20. G. R. Fowles, “*Introduction to Modern Optics*”, Dover Publications, Second Edition, 227 – 228, 1975.
21. <http://www.uniongas.com/aboutus/aboutng/composition.asp>
22. <http://en.wikipedia.org/wiki/Biogas>
23. T. Buxton, J. Campbell, “*Compressibility Factors for Lean Natural Gas-Carbon Dioxide Mixtures at High Pressure*”, Society of Petroleum Engineers Journal, 41st Annual Fall Meeting, Dallas, Texas, Oct 2 – 5, 1966.
24. C. Brown, “*Optical BTU Sensor Development – Final Report*”, technical report no. GRI-93/0083, Gas Research Institute, Chicago, IL under Contract No. 5034-271-1197, 1993.

25. O. C. Mullins, N. B. Joshi, H. Groenzin, T. Daigle, C. Crowell, M. T. Joseph, and A. Jamaluddin, "*Linearity of Near-Infrared Spectra of Alkanes*," Applied Spectroscopy, 54, 624 – 629, 2000.
26. M. A. VAN Agthoven, G. Fujisawa, P. Rabbito, and O. C. Mullins, "*Near-Infrared Spectral Analysis of Gas Mixtures*", Applied Spectroscopy, 56, 593 – 598, 2002.
27. R. J. Hayward and B. R. Henry, "*A General Local Mode Theory for High Energy Polyatomic Overtone Spectra and Application to Dichloromethane*", Journal of Molecular Spectroscopy, 57, 221-235, 1975.
28. S. W. Sharpe et al, "*Gas-Phase Databases for Quantitative Infrared Spectroscopy*", Applied Spectroscopy, 58, 1452 – 1461, 2004.
29. L. L. Gordley, B. T. Marshall and D. A. Chu, "*LINEPAK: Algorithms for modeling spectral transmittance and radiance*", Journal of Quantitative Spectroscopy and Radiative Transfer, 52, No. 5, 563-580, 1994.
30. T. Naes, T. Isaksson, T. Fearn, and T. Davies, "*A User-Friendly Guide to Multivariate Calibration and Classification*", NIR Publications, Chichester, UK, 27 – 37, 2002.
31. H. Valentine, "*Using the quasiturbine to regulate natural gas pipeline pressure and flow rate*", Energy Pulse, October, 2005.
[\[http://quasiturbine.promci.qc.ca/QTGasPipelineValentine0508.htm\]](http://quasiturbine.promci.qc.ca/QTGasPipelineValentine0508.htm)
32. R. C. Nelson, E. K. Plyler, and W. S. Benedict, "*Absorption Spectra of Methane in the Near Infrared*", Journal of Research of the National Bureau of Standards, 41, 615 – 621, 1948.

33. A. J. Rest, R. Warren, and S. C. Murray, “Assignment of the overtones and combination bands of liquid methane across the near infrared spectrum”, *Spectrochimica Acta Part A*, 52, 1455 – 1463, 1996.
34. L. P. Giver, “Intensity measurements of the CH_4 bands in the region 4350 Å to 10600Å”, *Journal of Quantitative Spectroscopy and Radiative Transfer*, 19, 311–322.
35. G. Pierre, J. Hilico, C. D. Bergh, and J. Maillard, “The Region of $3\nu_3$ Band of Methane”, *Journal of Molecular Spectroscopy*, 82, 379 – 393, 1980.
36. D. L. Gray and A. G. Robiette, “Extended Measurement and Analysis of the ν_3 Infrared Band of Methane”, *Journal of Molecular Spectroscopy* 77, 440 – 456, 1979.
37. C. Frankenberg, T. Warneke, A. Butz, I. Aben, F. Hase, P. Spietz, and L. R. Brown, “Methane spectroscopy in the near infrared and its implications on atmospheric retrievals”, *Atmospheric Chemistry and Physics Discussions*, 8, 10021 – 10055, 2008.
38. T. Momose, M. Miki, T. Wakabayashi, and T. Shida, “Infrared spectroscopic study of rovibrational states of methane trapped in parahydrogen crystal”, *Journal of Chemical Physics*, 107, 7707 – 7716, 1997.
39. H. G. Kjaergaard, et al., “Intensities in local mode overtone spectra: Propane”, *Journal of Chemical Physics*, 93, 6239 – 6248, 1990.
40. O. C. Mullins, R. J. Schroeder, and P. Rabbito, “Effect of high pressure on the optical detection of gas by index-of-refraction methods”, *Applied Optics*, 33, 7963 – 7970, 1994.

41. A. Sheeline, D. M. Coleman, and J. P. Walters, “*Experimental characterization of straight spectrometer slits*”, *Spectrochimica Acta* 34B, 43 – 53, 1978.
42. P. Spietz, J. Carlos G. Martin and J. P. Burrows, “*Quantitative treatment of coarsely-binned low resolution recordings in molecular absorption spectroscopy*”, *Spectrochimica Acta Part A: Molecular and Biomolecular Spectroscopy* 64, 722 – 735, 2006.
43. D. W. Berreman, “*Unfolding Spectrometer Slit Broadening Effects from Broad Spectra*”, *Applied Optics* 7, 1447 – 1453, 1968.
44. C. W. Brown, et al., “*Novel Sampling Device for Obtaining Process Near-Infrared Spectra of High-Pressure Gases*”, *Applied Spectroscopy*, 52, 746 – 749, 1998.
45. H. J. Achtermann, T. K. Bose, H. Rogener, and J. M. St-Arnaud, “*Precise Determination of the Compressibility Factor of Methane, Nitrogen and Their Mixtures from Refractive Index Measurements*”, *International Journal of Thermophysics*, 7, 709 – 720, 1986.
46. B. I. Lee and M. G. Kesler, “*A Generalized Thermodynamic Correlation Based on Three-Parameter Corresponding States*”, *AIChE Journal* 21, 510, 1975.
47. J. A. Rushing, K. E. Newsham, and K. C. Van Fraassen, “*Natural Gas z-Factors at HP/HT Reservoir Conditions: Comparing Laboratory Measurements with Industry-Standard Correlations for a Dry Gas*”, *SPE Gas Technology Symposium, Canada*, June 16 – 19, 2008.
48. S. G. Ghedan, M. S. Aljawad and F. H. Poettmann, “*Compressibility of natural gases*”, *Journal of Petroleum Science and Engineering*, 10, 157 – 162, 1993.

49. A. M. Elsharkawy, “*Efficient methods for calculations of compressibility, density and viscosity of natural gases*”, Fluid Phase Equilibria 218, 1 – 13, 2004.
50. Q. Li and T. Guo, “*A study on the supercompressibility and compressibility of natural gas mixtures*”, Journal of Petroleum Science and Engineering, 6, 235 – 247, 1991.
51. Kh. Nasrifar and O. Balland, “*Prediction of thermodynamic properties of natural gas mixtures using 10 equations of state including a new cubic two-constant equation of state*”, Journal of Petroleum Science and Engineering, 51, 253 – 266, 2006.
52. O. L. Noe, J. Goyette, T. K. Bose, and D. Ingrain, “*Determination of the compressibility factor and measurement of traces of water in methane by a microwave method*”, Fluid Phase Equilibria, 114, 135 – 145, 1996.
53. J. A. Schouten, J. P. J. Michels, and M. Jaeschke, “*Calculation of the Compressibility Factor of Natural Gases Based on the Calorific Value and the Specific Gravity*”, International Journal of Thermophysics, 11, 145 – 156, 1990.
54. M. N. Al-Khamis, “*Evaluations of Correlations for Natural Gas Compressibility Factors*”, MS thesis, King Fahd University of Petroleum and Minerals, Saudi Arabia, 1995.
55. J. Haugen, O. Tomic and K. Kvaal, “*A calibration method for handling the temporal drift of solid state gas-sensors*”, Analytica Chimica Acta, 407, 23 – 39, 2000.
56. D. Karlis, G. Saporta, and A. Spinakis, “*A Simple Rule for the Selection of Principal Components*”, Communications in Statistics, 32, 643 – 666, 2003.

57. X. Tang and Y. Li, “*Selection of the Number of Principal Components Based on Fault Signal-to-Noise Ratio*”, Proceedings of the 7th World Congress on Intelligent Control and Automation, China, 2008.
58. O. C. Mullins, T. Daigle, C. Crowell, H. Groenzin and N. B. Joshi, “*Gas-Oil Ratio of Live Crude Oils Determined by Near-Infrared Spectroscopy*”, Applied Spectroscopy, 55, 197 – 201, 2001.
59. H. R. Juliani, J. Kapteyn, D. Jones, A. R. Koroch, M. Wang, D. Charles and J. E. Simon, “*Application of Near-infrared Spectroscopy in Quality Control and Determination of Adulteration of African Essential Oils*”, Photochemical Analysis, 17, 121-128, 2006.

APPENDICES

APPENDIX A1

This section describes the enhancements made to the existing sensor software, which was initially designed in LabVIEW 7.1. The software consists of three main components: main user interface server, database handling server and spectrometer server. The main UI server communicates with the spectrometer and database server. Each of these servers is a library of programs. Each server employs queued-state machine architecture. Each server program has a number of cases, which are executed in sequence depending on the pre-determined event priorities. The software was upgraded to LabVIEW 8.6, the latest version available. Also, the sensor hardware was upgraded from National Instruments FieldPoint to cDAQ chassis. It was necessary to implement the following important functionalities into the software to improve stability and accuracy of the sensor:

1. Correcting the absorbance spectra measured during calibration/testing to standard temperature and pressure conditions, as the heating value needs to be specified always at standard conditions.
2. Temporal drift correction algorithm
3. Accounting for the compressibility factor of a mixture using the algorithm described in *Chapter 5*
4. Capability to characterize landfill gas mixtures (methane and carbon dioxide)

These capabilities were implemented in the software by adding some new LabVIEW virtual instruments (VIs) and by changing the cases available in the existing main UI server. The

newly added programs are called by the main UI server during the execution of required events/cases. No changes were made to the spectrometer server or database handler. A summary of the changes made is described below.

For density and temporal drift correction, a new VI named “Density and temporal drift correction.vi” was added to the library. This VI is called for execution during each loop, after the spectral data is acquired from the spectrometer and before predicting the mixture properties. The acquired spectral data, named “Last absorbance spectrum”, considered wavelength range, measured pressure and temperature are passed as an input to this VI. The absorbance correction VI processes the input and passes the density and drift-corrected absorption spectrum to the main UI. The corrected absorption spectrum is then used to predict the fuel properties. The connector pane of this VI is shown below:

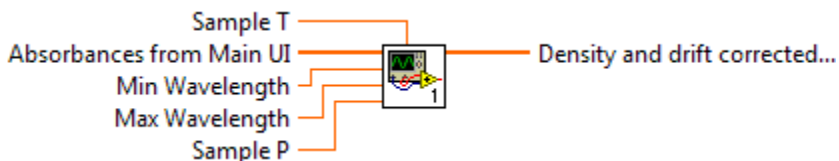


Fig. A1. 1 Absorbance correction VI - connector pane

The front panel and block diagram of the absorbance correction VI are shown below. The non-absorbing wavelength ranges to be considered for calculating the absorbance error can be changed directly in the front panel.

In order to make the program work for landfill gas mixtures, the number of components was changed to 3 (methane, carbon dioxide and nitrogen) from 5 (methane, ethane, propane, butane and nitrogen for natural gas mixture). The dimensions of all the affected arrays and matrices, such as, mean inputs and mean outputs matrices, regression coefficients, were modified accordingly. These changes span across a number of cases in the software, hence it is not feasible to show all the block diagram changes here.

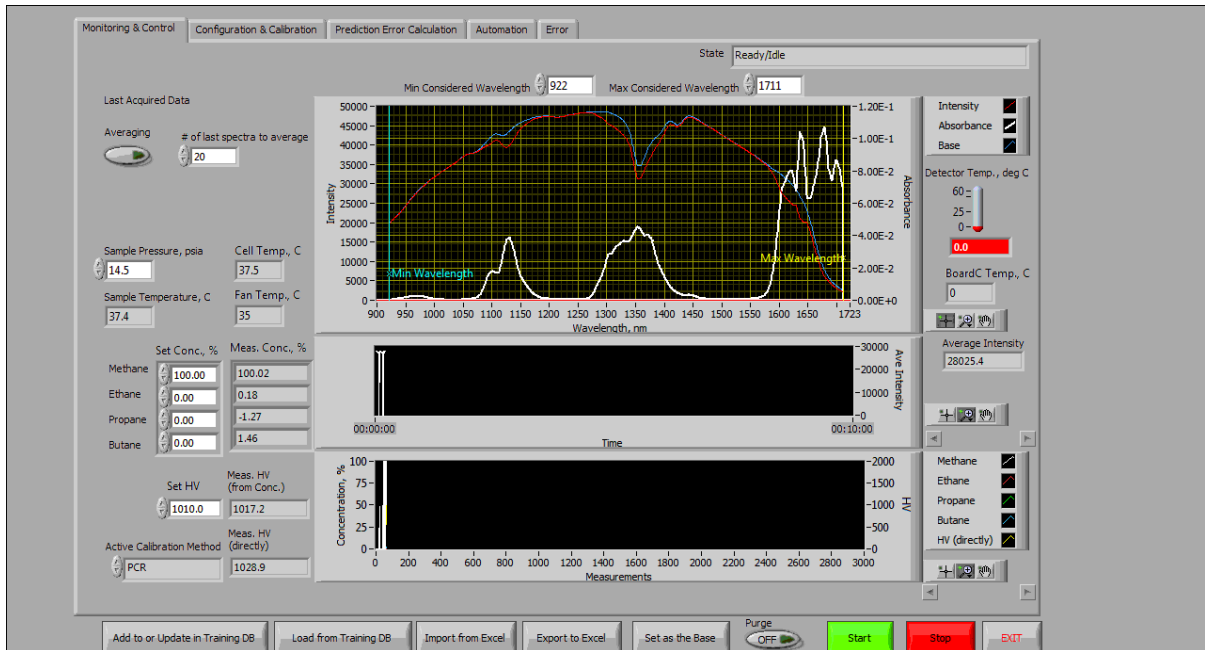


Fig. A1. 2 Main UI - front panel

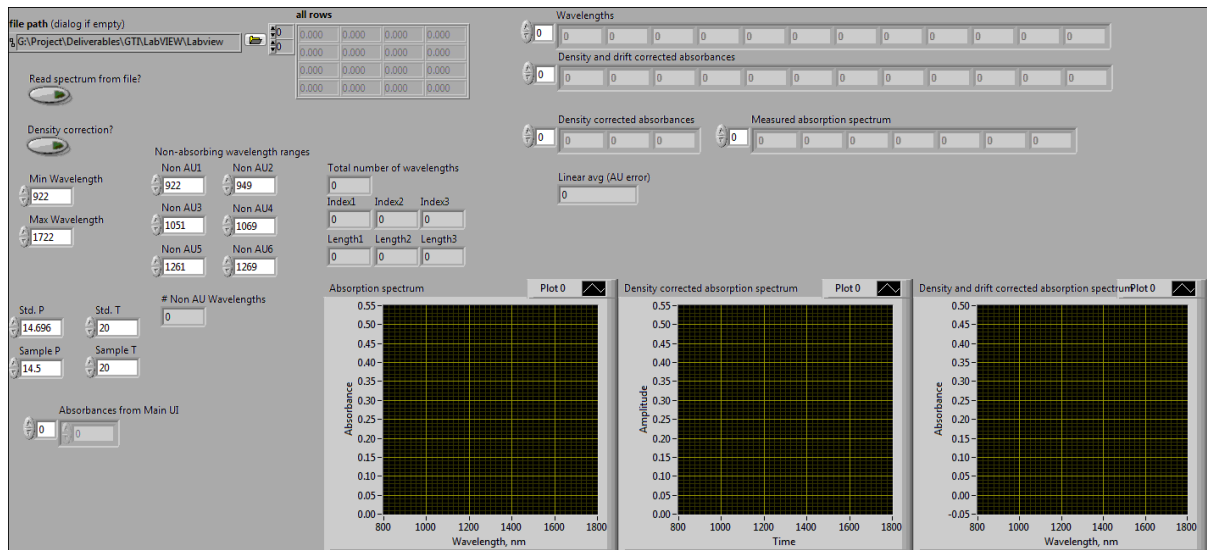


Fig. A1. 3 Absorbance correction VI - front panel